Preprint Cambridge Centre for Computational Chemical Engineering ISSN 1473 – 4273

Self-assembly of curved aromatic molecules in nanoparticles

Kimberly Bowal [1], Jacob W. Martin [1,2], Markus Kraft [1,2,3]

released: 15 February 2021

[1] Department of Chemical Engineering
and Biotechnology
University of Cambridge
West Site, Philippa Fawcett Drive
Cambridge, CB3 0AS
United Kingdom
E-mail: mk306@cam.ac.uk

[2] Cambridge Centre for Advanced Research
and Education in Singapore (CARES)
CREATE Tower, 1 Create Way
Singapore, 138602

[3] School of Chemical and
Biomedical Engineering
Nanyang Technological University
62 Nanyang Drive
Singapore, 637459

Preprint No. 267

Keywords: curved polycyclic aromatic hydrocarbon, nanoparticle, self-assembly, internal structure, mesophase

Edited by
Computational Modelling Group
Department of Chemical Engineering and Biotechnology
University of Cambridge
West Site, Philippa Fawcett Drive
Cambridge, CB3 0AS
United Kingdom

Fax: + 44 (0)1223 334796
E-Mail: c4e@cam.ac.uk
World Wide Web: http://como.cheng.cam.ac.uk/

Abstract

The self-assembly and structure of nanoparticles containing curved polycyclic aromatic hydrocarbon molecules (cPAHs) are investigated using molecular modelling. These polar fullerene-like molecules are receiving increased attention recently due to the steric and electronic properties caused by the inclusion of five-membered ring(s) within their hexagonal lattice. In this work, the curPAHIP potential is extended to describe the interactions between large cPAHs. It is then used within molecular dynamics simulations to produce nanoparticles containing cPAHs. Structural and energetic metrics, including diameter, density, intermolecular spacing, coordination number, alignment angle, radial distance, and energy value, are used to analyse systems containing cPAHs of different sizes and ratios, and containing flat PAHs or ions. Homogeneous cPAH particles are more tightly packed than their flat PAH counterparts, with large cPAHs displaying stacked columnar configurations absent in nanoparticles containing small cPAHs. Mixing cPAHs of different sizes disrupts the ordered mesophase and forms a core-shell structure in which the larger molecules make up the core and the smaller molecules comprise the shell, although this partitioning is less distinct compared to flat PAHs. In addition, the presence of flat PAHs and ions within cPAH nanoparticles promotes distinct arrangements dominated by weak dispersive interactions and strong electrostatic interactions, respectively.

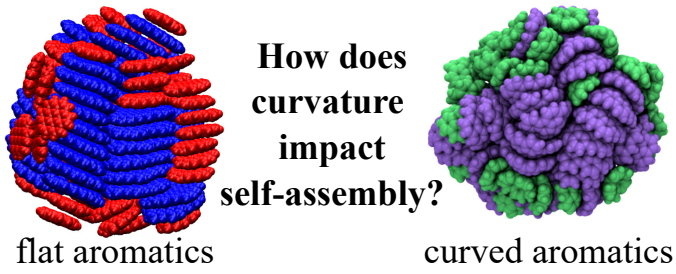

Highlights:

- Self-assembly is primarily dependent on cPAH size rather than particle size
- Different cPAH sizes disrupt mesophase formation and arrange in a core-shell particle
- Systems containing cPAHs and fPAHs self-assemble into janus particles
- Cations promote or disrupt particle structure depending on the constituent cPAH size

Contents

1 Introduction

Curved carbon structures are found in many materials including porous carbons, glassy carbons, activated carbons [31, 49, 50], and combustion carbons [47]. For example, high resolution transmission electron microscopy of energy-relevant carbon materials such as coke and soot shows that a significant proportion (63% for young particles, 28-49% for mature carbons) of the constituent molecules are curved [47, 81, 86]. This curvature is predominantly caused by the presence of non-hexagonal rings, such as pentagons, within a hexagonal lattice [48]. The resulting molecules, known as curved polycyclic aromatic hydrocarbons (cPAHs), have steric and electronic properties not present in defect-free carbon materials containing hexagonal structures only (flat polycyclic aromatic hydrocarbons, fPAHs). In particular, the curvature redistributes electronic charge in the π-cloud and causes the molecules to possess a dipole moment due to the flexoelectric effect [46]. This allows curved molecules to interact in long-range electrostatic interactions not present in systems containing planar carbon molecules, while still retaining aromaticity and showing considerable electron delocalisation [22, 27].

These qualities cause the presence of curved aromatic molecules to influence material structure and properties. Curved molecules increase material porosity [31] and facilitate stronger adsorbate-adsorbent interactions [46] which, combined with high polarisability and high surface area, provide enhanced adsorption important for applications such as carbon sequestration, gas storage, and separation [66]. Curved aromatics also possess a combination of properties, including surface charge stabilisation, high charge mobility, significant dipole moment, and small band gap [52] that make them excellent candidates for applications such as optoelectronic devices, organic semiconductors, liquid crystals, electrodes, imaging probes, and batteries [61]. For example, integrating corannulene inside insulating porous scaffolds allows electronic properties to be tuned and results in a 10,000-fold conductivity enhancement [60]. Flame-formed carbon nanoparticles show quantum dot behaviour [44]; quantum dots have shown great promise in bioimaging as well as photovoltaic and light emitting applications due to their tunability, biocompatibility, luminosity, and solubility [85].

Accurately describing and characterising the self-assembly and nanostructure of curved carbon materials is of interest to processes producing these desirable materials and also more broadly since curvature is easily integrated even when unintended. Many ubiquitous materials, such as combustion-produced pollutants [47], interstellar medium [45], and graphite synthesised from mesophase pitch, are only fully characterised when the influence of curvature is understood. In particular, the degree of molecular alignment to form columnar or stacked structures plays a significant role in the mechanical and electronic properties of materials, such as high electron transport characteristics desirable for organic electron devices [80] and the generation of graphisiting material. Previous work shows that fPAHs assemble in a nanocluster with good molecular alignment, forming an ordered mesophase [7, 17]. In contrast, the presence of curved molecules appears to contribute to a low degree of molecular ordering in a material [86] and prevent graphitisation of carbonised material by disrupting the formation of the mesophase [2], but to date no direct evidence has been provided for this.

Previous work on the structure and properties of materials containing polycyclic aro-

matic hydrocarbons has focused on fPAHs [18, 28, 32, 58], with less attention given to cPAHs. Electronic structure calculations show that there are significant interactions between nested concave-to-convex homogeneous cPAH dimers [13, 73] and, as with fPAHs, cPAH interactions are dominated by π-π dispersion interactions with weaker contributions from CH-π electrostatic interactions. That being said, electrostatics are more significant for cPAH interactions compared to non-polar fPAHs due to their permanent dipole moments [13, 37]. Different degrees of curvature result in increased or decreased cPAH dimer strengths, depending on the interplay of geometry and electrostatic effects. Curvature is able to increase interaction strength by decreasing C-C distances for increased dispersion interactions [41] but very curved molecules can also experience increased steric hindrance [48, 73] and increased exchange-repulsion that serve to destabilise the dimer [41, 73].

X-ray crystallography and density functional theory calculations have shown that the crystal structure of cPAH systems are determined by an interplay of electrostatic and dispersive forces, but predicting the packed structure of cPAHs is not straightforward. A molecule's dipole moment and molecule bowl depth are identified as significant factors, but do not have clear threshold values that guarantee particular molecular arrangements [24]. In addition, the size [25, 82], curvature [11, 56, 63], rigidity [74, 80], functionalisation [65], and atomic composition [35] of cPAHs are known to influence their ability to form columnar stacks in solid state. These systems often show large π-π overlap and staggered stacked interactions to produce extended π networks enhanced by CH-π interactions.

Preliminary work of larger molecular systems suggests that the self-assembly of homogeneous cPAH clusters is significantly different from similarly sized fPAH clusters [9], which may be due to the ability of polar cPAHs to engage in electrostatic interactions. Computational studies show that the binding energies between fPAHs of different sizes are weaker than those within a homogeneous system containing one molecule size [58]. This heterogeneity decreases the stability of a nanoparticle containing different molecule sizes and leads to a distinct partitioning in which the larger molecules formed the cluster core and the smaller molecules resided in the outer shell [7]. The extent to which this nanostructure is also seen within cPAH systems has not yet been investigated, but dimer calculations suggest that bowl complementarity may produce different behaviour by enhancing the stability of heterogeoneous cPAHs clusters [13]. Previous work has also characterised the first solvation shells of fPAHs around an alkali-metal ion [4, 9, 16], but this has not been well-explored for cPAHs, which would likely self-assemble differently due to their polarity. It is therefore of great interest to understand how the fundamental interaction differences in shape and binding behaviour between fPAHs and cPAHs may influence their self-assembly in homogeneous and heterogeneous nanoparticles. To date, detailed studies of cPAHs have primarily included electronic structure calculations or crystal structure experiments, as described above, neither of which provide information about intermolecular dynamics and particle nanostructure. Previous work looking at systems containing cPAHs and fPAHs show the effect of structure on porosity and adsorption [21, 84], but do not evaluate the system dynamics that are crucial to understand self-assembly and structural properties. In addition, most work does not include the flexoelectric effects so long-range dipole-dipole electrostatic interactions are not included.

The purpose of this work is to explore the self-assembly and internal nanostructure of clusters containing cPAHs, with the aim of answering the following questions relevant to carbon scientists: *What is the energy and structure of cPAH nanoparticle systems and how do these differ from systems containing fPAHs? What is the influence of particle size, molecule size and proportion, and presence of ions or fPAHs?* We address these by extending a force field parameterised for cPAH systems and using it within molecular dynamics simulations to provide a detailed assessment of cPAH cluster self-assembly.

2 Methods

2.1 Systems

To thoroughly evaluate the self-assembly of nanoparticles containing cPAHs, three different molecule types with different sizes and degrees of curvature are considered: a small fPAH containing seven hexagonal rings (coronene, $C_{24}H_{12}$), the smallest cPAH, which contains one central pentagonal ring with five surrounding hexagonal rings (corannulene, $C_{20}H_{10}$), and a larger cPAH containing two embedded pentagonal rings based on HRTEM analysis of early soot nanoparticles [47] ($C_{42}H_{14}$), all shown in Figure 3. The notation X_y is used to describe the clusters studied, where X values refer to the molecule type(s) and y gives the number of each type of molecule within the cluster. The molecule species considered in this work are referenced using the following letters: corannulene is indicated as A, $C_{42}H_{14}$ as B, coronene as C, circumcoronene (fPAH $C_{54}H_{18}$) as D, and potassium cation as K. For example, $A_{50}B_{50}$ indicates a cluster containing 100 molecules, made up of 50 corannulene and 50 $C_{42}H_{14}$ molecules.

The influence of particle size, molecule size, molecule curvature, molecule ratio and ion interactions are evaluated by considering 17 different clusters. Homogeneous clusters containing 25, 50, 100 and 200 of A and clusters containing 25, 50 and 100 of B are studied to provide information across molecule and cluster sizes. A series of heterogeneous clusters each containing 40 molecules of different sizes and proportions (A and B in proportions of 30:10, 20:20 and 10:30 are studied) allows evaluation of heterogeneity effects. In addition, a heterogeneous cluster containing 50 A and 50 B addresses heterogeneous cluster size effects. Clusters containing 20 A and 20 C provide insight into the interactions between cPAHs and fPAHs, and clusters containing 40 A or B with one or two potassium cations allow investigation into the self-assembly of ion-containing clusters. Snapshot images of each cluster considered in this work are shown in Figure 3. We should note that in this work, the terms (nano)particle and cluster are effectively synonymous: a nanoparticle is a cluster of molecules.

2.2 Force field development

Before any simulations can be conducted, the suitability of an intermolecular potential must be thoroughly evaluated. The isoPAHAP potential is an all-atom isotropic intermolecular description developed for fPAHs [77]. It was developed using high accuracy

benchmark quantum calculations and has been used in dynamic and stochastic simulations of fPAH systems [8, 28, 53, 78]. This potential uses fixed atom-centred charges, which are suitable for fPAHs where electrostatic interactions arise principally from the terminal groups. It is not able to capture local dipole moments located at strained internal carbon sites within cPAHs. Therefore we recently developed a new atomic potential for cPAHs, called the curPAHIP potential [9]. The curPAHIP potential models the increased polarity of cPAHs using a modified molecule description with off-site point charges located above the pentagonal carbon atoms and optimised potential parameters parameterised to SAPT(DFT) energies.

Previous work introducing the curPAHIP potential included the cPAH A only. In this work, we extend the molecular description to include the larger cPAH B and assess the suitability of the curPAHIP potential for the new systems. Following the parameterisation method developed for A in Bowal et al. [9], the geometry of B is minimised and massless charges are added 0.052 nm above each of the pentagonal carbon atoms to match the calculated dipole moment of 5.28 debye [47]. The resulting atomic coordinates and charges of the minimised B monomer (as well as A) are provided in Supplementary Information section A.1.

The binding energies of cPAH dimers are calculated to assess the suitability of curPAHIP in describing systems containing larger cPAHs. Density functional theory (DFT) calculations performed with the Gaussian 16 software [26] are used to determine the geometry of cPAH monomers and geometries and energies of cPAH dimers using a methodology similar to that used by Martin et al. [48] (see Supplementary Information section A.2 for details). Binding energies are shown for four dimers in Figure 1, compared with intermolecular potential curves calculated using the software ORIENT [71]. The energy computed with the isoPAHAP potential is included to highlight the behaviour of a potential, developed for fPAHs, that does not include the enhanced electrostatics and dispersion due to the flexoelectric effect and increased polarisability, respectively, and in all cases the isoPAHAP potential significantly underestimates the binding energy and overestimates the equilibrium dimer distance. The curPAHIP potential agrees well with the DFT and SAPT(DFT) results for the A dimer, see Figure 1(a). This is expected since these *ab initio* values were used in the parameterisation of the curPAHIP potential [9]. Figure 1(b) shows that the curPAHIP potential can be extended to cPAH molecules larger than A, since there is good agreement (within 5% of the dispersion-corrected DFT energies) for the larger B. In contrast, the isoPAHAP gives a minimum energy value that is 31% smaller than the DFT calculations. The energies of heterogeneous dimers, containing one A and one B, are also well captured by the curPAHIP potential, as seen in Figure 1(c) and (d). The repulsive branch of the curPAHIP potential is slightly shifted to smaller distances than the DFT values in some cases, which is acceptable since the repulsive branch still possesses the same mathematical form that has been found to produce appropriate cluster morphologies [53].

Comparing the DFT and curPAHIP potential results provides insight into the potential error in structural metrics of molecule arrangements calculated using the curPAHIP potential. The A dimer shows no significant deviation between the methods, which is expected since these molecule were used in the parameterisation of the potential. For dimers containing B, there is a slight overall shift of around 0.02 nm between the curPAHIP po-

tential energies and those calculated using DFT, which provides an estimate of the error in the intermolecular spacings determined in simulations using the cPAH intermolecular potential.

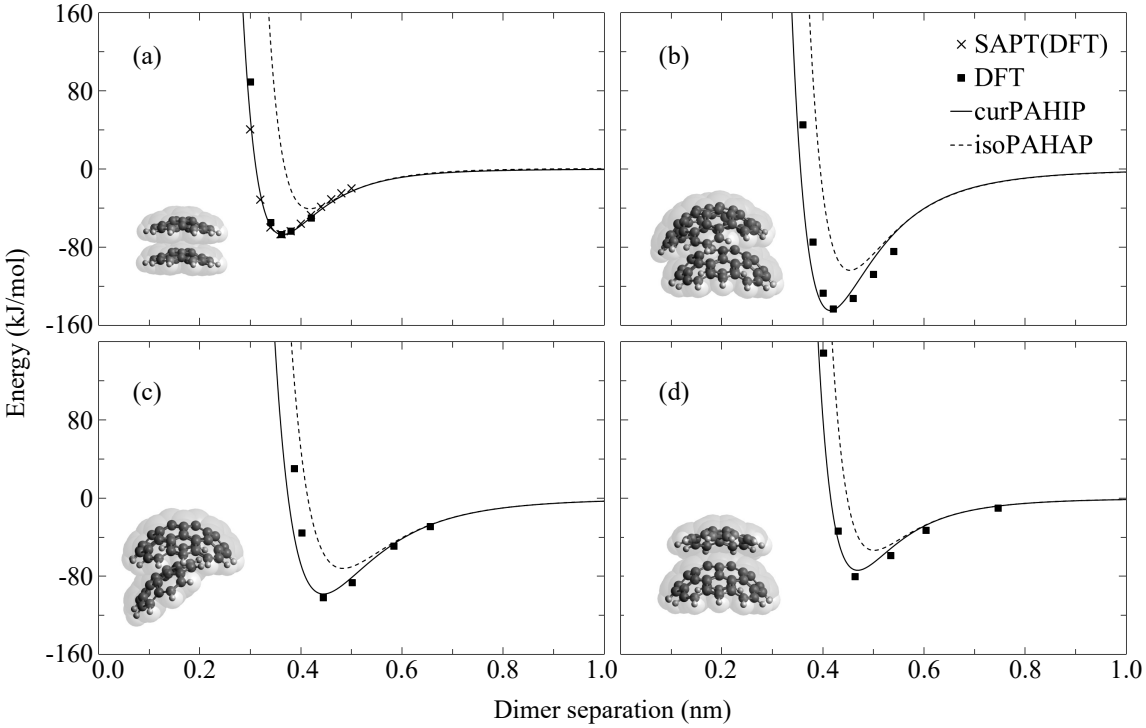

Figure 1: *Interaction energy versus separation distance for cPAH dimers determined from SAPT(DFT) calculations [13], DFT calculations, the curPAHIP potential, and the isoPAHAP potential. The dimers are as follows: (a) two A, (b) two B, (c) and (d) one A and one B each.*

Figure 1 focuses on sandwich type interactions between cPAH dimers although the nested dimer with the smaller A on the concave side of the larger B (Figure 1(c)) shows some T-shaped interaction. The ability of these intermolecular potentials to capture CH-π interactions is further explored with the T-shaped dimers of A and the fPAH C in Figure 2. We see that these interactions are weaker than their sandwich counterparts but there is good agreement between the potentials and the electronic structure calculations. The A dimer in which the molecules interact at the convex surface (Figure 2(a)) shows the same behaviour as the C T-shaped dimer. In addition, the isoPAHAP and curPAHIP potentials show similar trends (within 7% of each other) for all T-shaped dimers. This suggests that the increased interaction strengths and decreased binding distances observed for the dimer in which the molecules interact at the concave surface (Figure 2(b)) compared to the dimer involving interactions at the convex surface (Figure 2(a)) are due to sterically-enhanced dispersion rather than enhanced electrostatic interactions from the flexoelectric dipole. Importantly, we see that the T-shaped A dimer at the concave surface is stronger by 10 kJ/mol (over 30% enhancement) than the T-shaped interaction of fPAH C. This enhanced interaction allows T-shaped interactions to be energetically favoured over sandwich interactions when many corannulene molecules are considered, such as in a cluster

or bulk system.

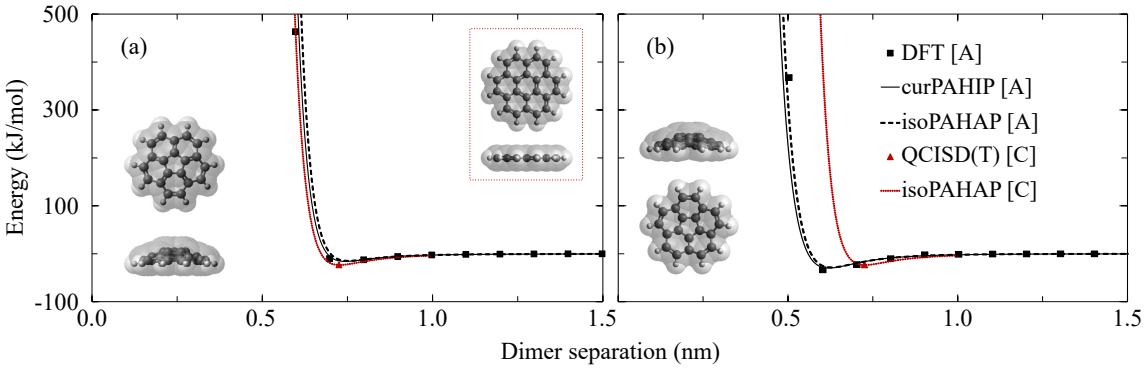

Figure 2: *Interaction energy versus separation distance for cPAH and fPAH dimers in T-shaped configurations determined from QCISD(T) calculations [36], DFT calculations, the curPAHIP potential and the isoPAHAP potential. Square brackets indicate the corresponding molecule types for each calculation method. The T-shaped dimer interactions with (a) the convex surface and (b) the concave surface of A are compared with the T-shaped C dimer, which is pictured in the dotted inset.*

Further details on the isoPAHAP and curPAHIP potential form and parameters are found in Supplementary Information section A.3. For simulations considering both fPAHs and cPAHs in a single cluster, the curPAHIP potential was used to describe the mixed molecule interactions and simulations. Using the isoPAHAP potential to describe these interactions showed very similar results.

2.3 Molecular dynamics

Cluster configurations are produced using a multi-step molecular dynamics simulation process. Clusters are initialised in a mixed configuration, with molecules randomly placed within a large spherical volume using the PACKMOL software [51]. Excess energy is removed by an energy minimisation step using the steepest descent algorithm, followed by the low-memory Broyden-Fletcher-Goldfarb-Shanno method [12].

Replica Exchange Molecular Dynamics (REMD) simulations are used to rapidly produce equilibrated cluster systems. Modelled after Monte Carlo parallel tempering [33], REMD is an advanced form of molecular dynamics that involves evaluating simultaneous isothermal systems, called replicas, across a temperature range [72]. At regular intervals throughout the simulation, neighbouring replicas are able to exchange spatial information based on a Boltzmann-weighted temperature dependent probability. This method allows efficient and rapid sampling of the potential energy landscape of the system since low energy replicas are able to explore new configurations generated by higher energy replicas.

In this work, REMD simulations are conducted for 3 ns. A large temperature range is selected to include solid-like and liquid-like particle morphologies. For clusters containing only A, only B, A and B, and A and C this corresponds to temperature ranges of

200–800 K, 400–1600 K, 200–1600 K and 200–800 K, respectively. These require between 27 and 84 REMD replicas to maintain an acceptable replica exchange acceptance. Further information detailing the replica temperature selection and an assessment of effectiveness is given in Supplementary Information section A.4. As described in detail in similar work [7], a flat-bottomed spherical position potential is applied within the REMD simulations to address complete evaporation of small molecules from the cluster at high temperatures. Individual 1 ns simulations using classical molecular dynamics (MD) are then conducted at each desired temperature from the final REMD configurations. No position potential is implemented for these post-REMD MD simulations.

In the REMD and MD simulations the NVT ensemble, where a constant number of atoms, system volume and temperature are maintained, is sampled using a chain of 10 Nosé-Hoover thermostats for temperature control. A velocity Verlet integrator [79] is used to advance the configuration in 1 fs time steps and all simulations are conducted *in vacuo* without periodic boundary conditions. Intramolecular forces are determined using the OPLS-AA force field [39] for molecular bonds, angles, dihedral and improper dihedral angles. The curPAHIP intermolecular potential [9] is used to describe interactions between cPAHs and intermolecular cut-offs are set to 3.0 nm. All minimisation, REMD and MD simulations are conducted using GROMACS 5.1.4 [1]. Purpose-made scripts are used to the process the output and the software VMD [34] provides visualisations.

2.4 Structural analyses

A number of different metrics, including density, intermolecular spacing, coordination number, alignment angle and radial distance, are used to evaluate system structural properties. All metrics are averaged over the final 500 ps of the post-REMD MD simulation of the lowest temperature replica (*i.e.* 3.5–4.0 ns of total simulation time) using a timestep of 1 ps. Many calculations require the identification of near neighbours for each molecule within the system. For this, molecules are considered neighbouring if their centres of mass are within the cut-off radius R for at least half of the 500 ps production period. Unless otherwise stated, values of R are selected to allow $> 85\%$ of molecules to have at least one identified neighbour. This results in cut-off radii of $R_{\mathrm{A}} = 0.7$ nm, $R_{\mathrm{B}} = 0.5$ nm, and $R_{\mathrm{C}} = 0.5$ nm for PAH molecules A, B and C, respectively. The sensitivity of the cut-off values on calculated cluster properties is discussed in Supplementary Information section A.5.

Diameter and density values are determined using the solvent-excluded surface of the cluster calculated using a rolling sphere algorithm [64], as in previous work of fPAH clusters [10, 15]. This provides values that are more accurate than commonly used spherical approximations since they are directly calculated from the three-dimensional surfaces. Molecular alignment angles are calculated to provide information on the relative configurations of neighbouring molecules within the clusters studied. An alignment angle is defined as the angle between normal vectors to the central rings (for A this is the pentagonal ring and for B this is the central hexagonal ring) of the neighbouring cPAHs considered. Supplementary Information Figure A2 provides a schematic of the alignment angle between two neighbouring A molecules. A quantitative measure of the degree of stacking order in the molecular structures is provided through the use of coordination

numbers (CNs), calculated as the number of near neighbours averaged over each molecule type. To consider only π-π stacking interactions within this metric, different values of the cut-off R are selected such that sandwich-type stacked interactions between molecules are included in the calculations but molecules more than one layer away are excluded. Equilibrium dimer distances, at which their intermolecular energy is minimised, provide the cut-off values of $R_A = 0.4$ nm and $R_B = 0.5$ nm used in calculating the coordination numbers. Radial distance, r, is defined as the distance between a molecule type and the cluster centre averaged over all atoms and provides insight into the spatial partitioning of molecule types within a cluster, particularly useful for understanding the self-assembly of heterogeneous systems. Further information on the calculation of the radial distances and coordination numbers is provided in Supplementary Information section A.6.

3 Results and Discussion

Figure 3 shows all of the low energy cluster geometries and Table 1 provides a summary table containing the corresponding structural metrics. The discussion of these results will be structured around questions in materials and combustion science including:

- **Do cPAHs self-assemble into an ordered phase?** cPAHs clusters are analysed to explore the impact curvature has on the development of an ordered mesophase.
- **What is the internal nanostructure of cPAH particles?** cPAH clusters are evaluated with additional metrics (densities, radial distances and energetics) to explore properties particularly relevant to combustion-generated nanoparticle pollutants and nanoparticle synthesis.
- **How do complex cPAH particles self-assemble?** Clusters containing cPAHs with fPAHs or ions are structurally and energetically analysed to provide insights into real-world systems such as janus nanoparticles, battery materials and combustion-generated nanoparticles.

3.1 How do cPAHs self-assemble?

As mentioned, mesophase formation (the molecular alignment of aromatic molecules) is critical for graphitisation. The intermolecular spacing, coordination number and alignment angle values of molecules within homogeneous and heterogeneous clusters of cPAHs will be compared with similar clusters of fPAHs and experimental systems to provide insights into this question regarding cPAH self-assembly.

Average intermolecular spacing is an important experimental quantity when tracking the formation of a mesophase and subsequent graphitisation as well as the presence of curvature in combustion carbons [6]. The homogeneous cPAH clusters evaluated in this work have intermolecular spacings that do not change significantly with cluster size but depend strongly on the constituent molecule size. Clusters containing A possess an average intermolecular spacing of 0.59 nm while clusters containing B have an average spacing of

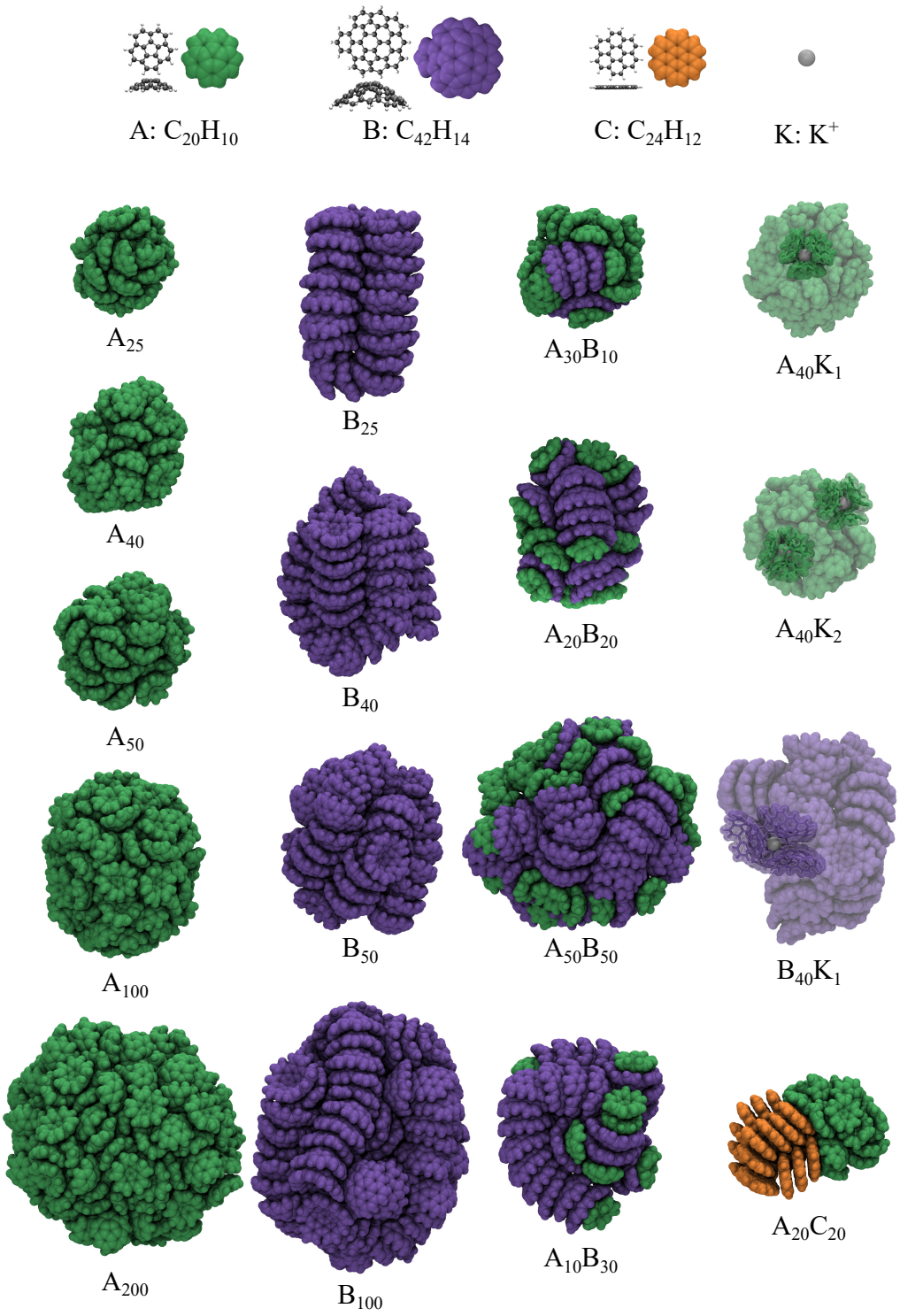

Figure 3: *Visualisations of the corannulene molecule (A, coloured green), $C_{42}H_{14}$ molecule (B, coloured purple), coronene molecule (C, coloured orange) and potassium cation (K, coloured grey), and clusters studied in this work. Ion-containing clusters are shaded to emphasise the solvation shell surrounding the ion(s).*

Table 1: *Cluster diameter, density, intermolecular energy, average intermolecular spacing, average coordination number (CN), and radial distance (r) of molecules A, B, and C for all clusters studied in this work.*

Cluster	Diameter (nm)	Density (g/cm^3)	Energy (kJ/mol molecule)	Spacing (nm)	CN (-)	r_A (nm)	r_B (nm)	r_C (nm)
A_{25}	2.36	1.50	-75	0.59	0.01	0.91	–	–
A_{40}	2.77	1.49	-82	0.59	0.02	1.07	–	–
A_{50}	3.00	1.47	-84	0.60	0.01	1.14	–	–
A_{100}	3.79	1.45	-92	0.59	0.00	1.46	–	–
A_{200}	4.79	1.45	-97	0.60	0.01	1.85	–	–
B_{25}	2.96	1.59	-144	0.44	1.57	–	1.27	–
B_{40}	3.49	1.55	-152	0.45	1.58	–	1.45	–
B_{50}	3.76	1.55	-157	0.45	1.43	–	1.49	–
B_{100}	4.77	1.52	-165	0.45	1.36	–	1.92	–
$A_{10}B_{30}$	3.31	1.58	-147	0.44	1.04	1.53	1.30	–
$A_{20}B_{20}$	3.16	1.55	-125	0.44	0.92	1.31	1.20	–
$A_{50}B_{50}$	4.31	1.52	-135	0.51	0.70	1.85	1.49	–
$A_{30}B_{10}$	2.98	1.52	-103	0.54	0.74	1.21	1.04	–
$A_{20}C_{20}$	2.88	1.46	-80	0.43	0.74	1.18	–	1.21
$A_{40}K_1$	2.78	1.49	-88	0.61	0.10	1.06	–	–
$A_{40}K_2$	2.79	1.48	-94	0.58	0.20	1.05	–	–
$B_{40}K_1$	3.50	1.54	-149	0.46	1.21	–	1.35	–

0.45 nm. This shows that the spacings within homogeneous clusters are controlled by the molecular composition of the cluster rather than the number of molecules in a cluster. Intuitively, one would expect the intermolecular spacing to increase with molecule curvature due to steric effects that prevent the molecules from interacting closely, however the opposite trend is observed. This suggests that these two cPAH molecule types configure in different arrangements that are not controlled solely by steric effects.

To provide a comparison to reference molecule arrangements, the spacings of cPAH dimers using electronic structure calculations from Figure 1 are (a) 0.36 nm, (b) 0.42 nm, (c), 0.44 nm, and (d) 0.46 nm. This shows that the average spacing of A within a homogeneous cluster is significantly larger than that of its sandwich dimer. The average intermolecular spacing within a single layer of the A crystal structure characterised by X-ray crystallography is 0.57 nm, suggesting the cluster structure of A likely possesses significant contributions from CH-π interactions, in which the more positive region at the rim of one molecule is almost perpendicular to the negative region and the bottom of another molecule in a T-shaped configuration, rather than tight sandwich interactions. Further information on the A crystal structure is provided in Supplementary Information section in the context of providing verification of our analysis calculations A.7. In contrast, the average intermolecular spacing of a B cluster is similar to that of its sandwich dimer and similar to the spacing found in crystal structures of similarly curved indenocorannulene species (0.34–0.37 nm [24]). The intermolecular spacings within clusters containing B

do not change readily with the cut-off distance used, indicating that B have distinct near neighbours, for example in a highly stacked configuration. In contrast, A spacings are strongly correlated to the cut-off distance selected, suggesting that the molecules are not arranged in structured stacked layers. Intermolecular spacings are reported for a number of cut-off distances in Supplementary Information Table A3.

The intermolecular spacings within heterogeneous cPAH clusters suggest that both the molecular ratio and cluster size play a role in the average spacing. This is investigated further in Table 2, which breaks down the average results by considering the molecule type contributions to the intermolecular spacing. The interactions between molecules of the same type maintain spacings similar to those in the homogeneous clusters, so that the spacings between A are larger than those between B. As in the homogeneous clusters, the B-B spacings are similar to that of a minimised B dimer and reasonably uniform across all heterogeneous clusters. Cluster size does not influence the A-A spacing, however the proportion of A plays a role. The mixed molecule interactions have similar spacings to those of the larger cPAH suggesting that B promotes the close stacking behaviour of π-π interactions with A. This is more pronounced in clusters with a higher proportion of B compared to A and is also cluster-size dependent. The differences between average spacings for the heterogeneous clusters (for example comparing $A_{20}B_{20}$ and $A_{50}B_{50}$) are therefore observed to be largely due to the number of neighbouring A or B within each cluster rather than the molecule type intermolecular spacings. This molecule type behaviour is likely due to the difference in curvature between these two cPAHs rather than the molecule sizes alone, since fPAH clusters containing a disparity of molecule sizes do not possess these differences (for example, a cluster containing 16 molecules each of the fPAHs C and D has an average spacing of 0.42 nm, with C-C spacings of 0.43 nm, C-D of 0.40 nm, and D-D of 0.41 nm [7]),

Table 2: *Intermolecular spacings within heterogeneous clusters, considering average distances between molecule types A and B.*

Cluster	B-B	B-A	A-A
$A_{10}B_{30}$	0.43	0.43	0.53
$A_{20}B_{20}$	0.43	0.41	0.61
$A_{30}B_{10}$	0.44	0.48	0.58
$A_{50}B_{50}$	0.44	0.47	0.60

These cPAH cluster intermolecular spacings are higher than those of systems containing planar carbons. For example, a cluster containing 100 fPAH C molecules [17] has an average intermolecular spacing of 0.43 nm while the cPAH clusters containing 100 molecules possess spacings between 0.45–0.59 nm. This is especially true for heterogeneous clusters, predominantly due to the fact that different fPAH molecule sizes possess similar spacing values unlike the cPAHs here. In flame-produced soot particles, the intermolecular spacings measured using high resolution transmission electron microscopy are between 0.38 and 0.48 nm, depending on the particle maturity [3, 6]. This range is similar to the values within found homogeneous and heterogeneous clusters containing B. These results suggest that clusters containing a significant proportion of A are not complete representations of these experimental systems.

Coordination number values (CNs) provide information on the extent of stacking interactions, which can help explain the intermolecular spacing results by identifying near neighbour patterns. In particular, this metric shows whether T-shaped interactions (in which molecules do not possess any near neighbours) or sandwich interactions (in which each molecule has one or two near neighbours) dominate. The homogeneous A clusters show an average CN of 0.01 $\pm$ 0.01, indicating predominantly T-shaped interactions, while the B clusters possess a CN of 1.48 $\pm$ 0.09, suggesting that they self-assemble with sandwich interactions. As seen in the cluster snapshots, B interact closely such that each molecular bowl inserts into the concave surface of its neighbour, allowing each molecule to possess on average more than one near neighbour in a stacked configuration. This is very similar to the arrangements of fPAH within clusters (for example, C_{100} has an average CN of 1.6 [18]) and cPAH hybrids that form tight stacks [23]. In contrast, A do not have near neighbours within stacking distance and the molecular bowls do not pack tightly within each other. As discussed by Liu et al. [44], molecular stacking is an important factor for the band gap of a PAH nanoparticle.

To further examine the influence of compositional heterogeneity, we compare CNs across different clusters each containing 40 cPAH molecules in Figure 4. The molecule-specific CNs within these heterogeneous clusters align with those calculated for homogeneous clusters. The B within all clusters have CNs above 1, indicating that on average these molecules have more than one near neighbour in a stacked arrangement. In contrast, all A have CNs significantly below 1, which shows that these molecules do not arrange in close stacks. This suggests that the formation of an ordered phase is more likely with larger cPAHs compared to small species such as A. This molecule type difference, where smaller molecules possess lower CNs than larger molecules within a cluster, is also seen in fPAHs (for example, CNs of 2.00 and 1.25 for the C and D, respectively, within a $C_{16}D_{16}$ cluster) and is linked to the presence of smaller PAHs on the cluster surface (often by capping the ends of molecule stacks) compared to the bulk-residing larger PAHs. The CNs for both cPAH sizes follow the trend $A_{40} < A_{30}B_{10} < A_{20}B_{20} < A_{10}B_{30}$ (shown with a solid arrow), illustrating that the addition of B into A clusters increases the degree of order and stacking.

We also are interested in which molecule types are present as near neighbours within these heterogeneous systems. We find that the CNs of A have no contribution from A, meaning that all A stacking interactions come from neighbouring B. The majority of B stacking interactions come from other B, however some of the interactions are with A in proportion to the molecular ratios within the cluster, shown as insets with horizontal lines in Figure 4. This highlights that the smaller cPAH A interacts most strongly in the concave surface of the larger cPAH B, in agreement with calculated DFT dimer energies and our previous suggestion that interactions between bowl-complementing heterogeneous cPAH dimers could remove the strict steric constraints limiting the interaction strengths of homogeneous cPAHs [48].

Figure 5 presents histograms of the molecular alignment angles, illustrating the relative configurations of neighbouring molecules within the homogeneous clusters studied. It is again immediately clear that the two molecule sizes behave differently but these trends are consistent across all cluster sizes considered (additional cluster size plots can be seen in Figures 6, A1 and A3). The systems containing B (in the top row) show a single

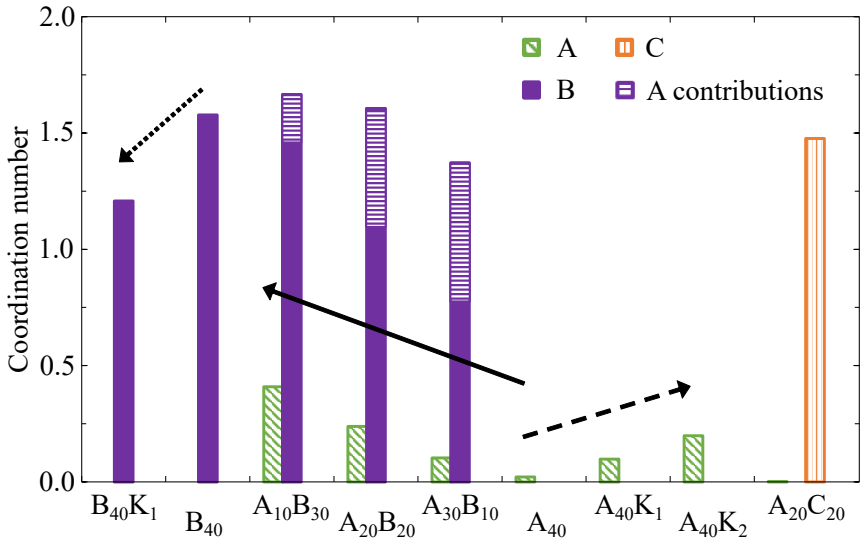

Figure 4: *Molecule type coordination number values for clusters containing 40 PAHs.*

significant peak around 20°. This suggests that nearly all of the molecules interact in a tilted stack formation, forming one dimensional columns in which the molecule bowls possess a concave-to-convex alignment with dipole moment vectors nearly aligned. This small alignment angle provides significant π-π overlap that, within columnar structures, is identified as a feature of materials with good performance in organic electronic devices. This dominant alignment angle is the same as that observed between a minimised B dimer (shown as a dashed vertical line), indicating that this is a stable arrangement. Similar self-assembled structures are observed in crystals containing indenocorannulene molecules [24] and other highly curved cPAHs that form polar crystals with strong photoluminescence [20]. Neighbouring columnar stacks of B have opposite bowl directions and weak CH-π interactions provide little interaction between columns. Interestingly, the columns show significant tilting at their ends such that parallel columns curve to be nearly continuous, which is not a feature of crystal structures and likely influences cluster surface properties. fPAH clusters, such as the representative C_{100} shown in Figure 5, show even sharper angle peaks, suggesting a strong mesophase formation. However, these peaks are centred around 0° and 180°, which both correspond to aligned molecular planes (since the alignment angle calculation uses a normal vector). The variance in the fPAH alignment angles are likely from shifted interacting molecular planes as well as small tilting angles. This π-π stacking arrangement combines with CH-π interactions to produce a herringbone-like structure within both clusters and bulk crystal fPAHs [42], without the column curving present in cPAH clusters.

In contrast, clusters containing A (bottom row of Figure 5) show a dominant but broad peak around 45°, with smaller wide peaks around 130° and 170°. This agrees with previous work that shows A do not pack with any long-range order [30, 40, 57, 67, 80] (the angles found in the crystal structure are shown as vertical dashed lines), with some CH-π interactions but limited π-π interactions. As seen in the dimer energies, the molecule shapes enhance the interaction energy of T-shaped dimers in these small cPAHs so that, in contrast to the preferred stacked structure of fPAHs, this configuration becomes favoured for extended systems. It is interesting that this bulk molecular arrangement is observed

even within the small nanocluster systems examined here. The method constraints of this work highlight that this structure is not due to the rapid bowl inversion dynamics or induced polarities within the system but instead to the molecule size, shape and electrostatic properties.

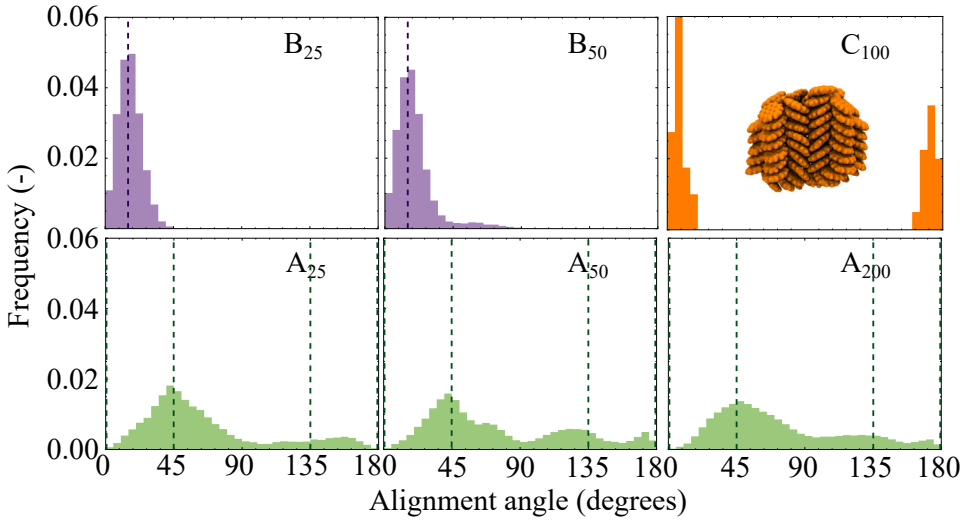

Figure 5: *Alignment angle distributions for homogeneous B and A clusters across different cluster sizes, with values for a fPAH cluster containing C included for comparison. Vertical dashed lines provide the angles found in the crystal structure (for A) and minimised dimer (for B).*

Given that the two molecule types self-assemble with different alignment angles, we explore how mixing these molecules influences the alignment angle distributions. Figure 6 (second row) shows heterogeneous clusters each containing 40 molecules alongside the corresponding homogeneous clusters (third row). Additional results from larger clusters are found in Supplementary Information Figure A3. In all heterogeneous clusters, the individual molecule alignment peaks align reasonably well with those seen in the homogeneous clusters, A crystal structure and B dimer, with the majority of B around 20° and many A around 45°. There is an additional small B peak around 45°, indicating some deviations from columnar stacking that align with the dominant arrangement of A. This is more pronounced in clusters containing $\geq$50% A, suggesting that A molecules are located within B columns. The molecule proportions also influence A angles, with shifts towards lower angles and reduced values around 130°. The $A_{30}B_{10}$ cluster shows a distribution similar to that of the homogeneous A cluster, although the peaks are much broader. As the proportion of B increases their influence is felt on A so that in the cluster containing equal ratios of both molecules ($A_{20}B_{20}$), the A peak at 45° is spread out towards 0° and the former 135° peak is pushed towards 170°. In the cluster containing 75% B ($A_{10}B_{30}$), the largest angle peak for A aligns with that of B at 20°. This indicates that A are stacking in a similar fashion to B, which can be seen in the corresponding cluster snapshot (Figure 3) where A predominantly interact individually at the ends of B stacks, fitting in the concave or convex surfaces. Although similar molecule size interactions are observed in heterogeneous fPAH clusters, these planar aromatics do not self-assemble with different alignments depending on molecule size and thus heterogeneous clusters show the same

highly aligned columnar stacking behaviour as homogeneous clusters, for example shown in the $C_{16}D_{16}$ cluster in Figure 6 (top row).

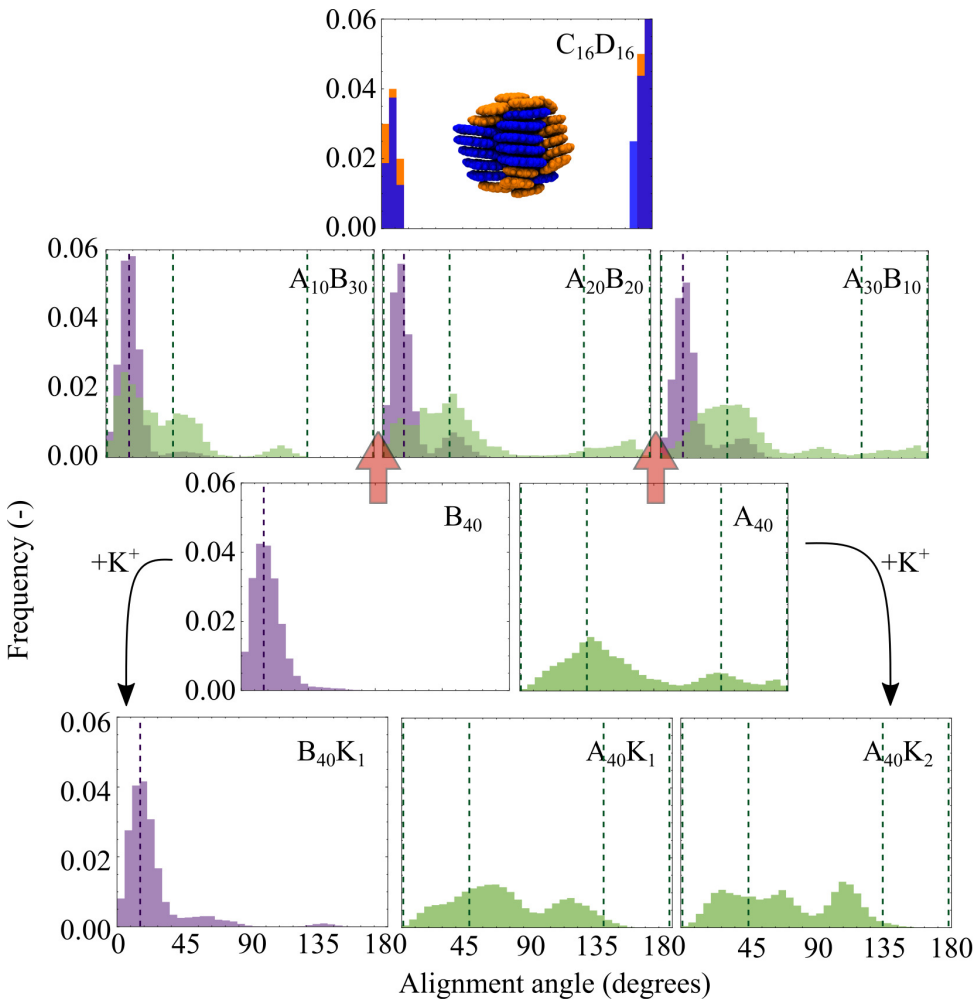

Figure 6: *Alignment angle distributions for A and B clusters containing 40 molecules. The third row shows the homogeneous clusters, with red arrows showing the heterogeneous clusters (second row) and curved arrows indicating ion-containing clusters (bottom row). Angle distributions for a heterogeneous fPAH cluster (top row) obtained from Bowal et al. [7] is provided for comparison (C coloured orange, D coloured blue).*

This detailed evaluation of intermolecular spacing, CNs and alignment angles shows that the self-assembly of cPAHs depends strongly on their molecular geometry and not the cluster size. Strong CH-π attractions between molecule rims and bowl centres control the arrangement of A while dipole-dipole attractions and dispersion interactions control the nanostructure of B clusters. This molecule size dependent structure is observed within the crystal structures of cPAHs and also influences the behaviour of heterogeneous systems. Systems containing B show high CNs and low alignment angles, suggesting good molecular alignment similar to clusters of fPAHs. However, cPAH clusters containing even small proportions of A disrupt mesophase formation.

3.2 What is the internal structure of cPAH nanoparticles?

Characterising the internal nanostructure of cPAH clusters provides valuable information relevant to the formation and composition of combustion-generated nanoparticles as well as the design of nanoparticles for optoelectronic applications. In this section we will discuss cluster densities and energies and will use radial distances to consider the partitioning behaviour of clusters containing different ratios of molecule sizes.

Cluster diameters and densities, reported in Table 1, show that cPAHs form tightly packed clusters. Homogeneous B clusters possess densities of 1.52–1.59 g/cm^3, which is comparable to mature graphitised soot particles (1.50–2.08 g/cm^3 [38]) although still significantly lower than graphite (2.09–2.23 g/cm^3). Cluster densities for A are between 1.45 and 1.50 g/cm^3, higher than that of the A crystal structure (1.36 g/cm^3 [57]) and comparably sized fPAH clusters (1.39–1.46 g/cm^3 [18]) but still within the range ascribed to young soot particles (1.12–1.50 g/cm^3 [14, 76]). All cluster densities decrease with increasing cluster size, although this effect is muted for cPAH clusters compared to their fPAH counterparts. The diameter and density values of heterogeneous cPAH clusters are consistent with simple mixing averages of the analogous homogeneous cPAH clusters, suggesting that heterogeneity does not cause a dramatic change in the overall cluster shape and packing.

We are particularly interested in whether cPAHs show the same core-shell partitioning seen in fPAH systems, where the cluster core consists of the larger fPAHs and the shell contains the smaller fPAHs, which has been suggested to explain the core-shell nanostructure seen in young combustion carbons [7]. Average radial distances between each molecule type and the cluster centre are calculated to provide an indication of the molecule type positioning within each cluster, tabulated in Table 1. For the homogeneous cases, the two molecule types show similar relative average radial distances at 77–85% of the total cluster radius, similar to the fPAH clusters (for example, C_{100} has a value of 77% [18]). However, in all clusters containing two molecule types A possess larger average radial distances (located within 80–90% of the total cluster radius) than B (70–80% of the cluster radius). This is indicative of a core-shell structure in which the larger molecules reside in the cluster core, as seen in fPAH clusters (for example, the average radial distances of C and D are 89% and 65% of the cluster radius, respectively, for $C_{16}D_{16}$ [7]).

Although the average radial distances show a core-shell partitioning of molecule sizes, the distribution of radial distances shows that this radial separation is less distinct for clusters containing cPAHs compared to similar fPAH clusters. Figure 7 shows that there is significant mixing of the molecule types within the cPAH clusters and molecules of both types are present near the cluster centre, regardless of cluster size or molecular ratio. This core-shell structure confirms that like fPAH clusters, cPAH clusters show the inverse molecular arrangement compared to that observed experimentally for mature combustion particulates [6], indicating that the core-shell nanostructure arises from carbonisation rather than physical partitioning of different sized PAHs.

We previously explored the contribution of flexoelectrically polarised aromatics to soot formation [47] and it follows that long-range dipole-dipole interactions between cPAHs may allow cPAH clusters to possess increased stability compared to fPAHs. This would be of particular interest to contexts in which stable PAH nanoparticles are present, such

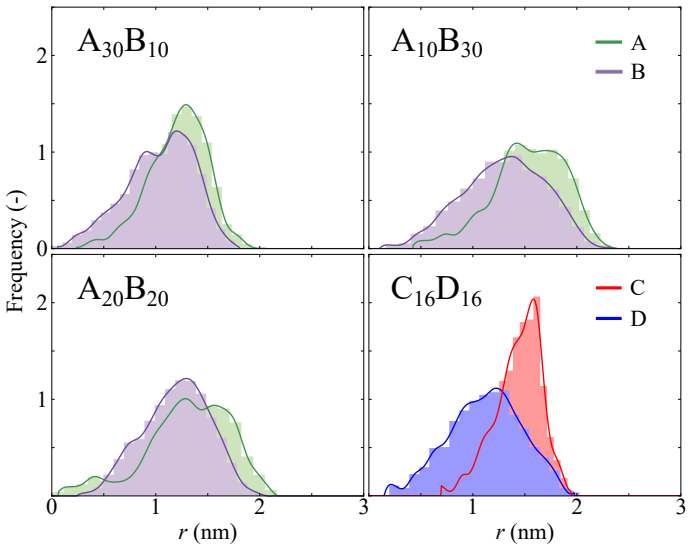

Figure 7: *Normalised atomic radial distance distributions for heterogeneous PAH clusters. The fPAH cluster $C_{16}D_{16}$ is obtained from Bowal et al. [7].*

as combustion and interstellar medium. To address this hypothesis, we present intermolecular energies as a function of mass for cPAH and fPAH clusters, shown in Figure 8. The energies are shown per atom in the system in order to facilitate direct comparison between systems of different cluster and molecule sizes. It is clear that in all cases the energy decreases with increasing cluster mass. Homogeneous clusters containing fPAHs (all coloured similarly here to allow for ease in reading), taken from Chen et al. [18, 19], show relatively consistent energy trends across molecule sizes from pyrene to circumcoronene, with heterogeneous clusters, taken from Bowal et al. [7], generally at lower energies. Clusters containing cPAHs tend to have lower energies than fPAHs, as predicted based on their increased electrostatic attraction, although this is dependent on cPAH cluster composition. Homogeneous clusters containing B show energies similar to those of heterogeneous fPAH clusters and A clusters possess lower mass-weighted energies. All cPAH clusters show significantly lower energies than the corresponding cPAH dimer interactions, which possess energies of -0.93 to -1.28 kJ/mol atom. For reference, the experimental binding energy of graphite is -3.4 kJ/mol atom with a large range from -2.4 to -4.8 kJ/mol atom [5].

The effect of heterogeneity in cPAH clusters shows a distinct effect of molecular ratio: an increased proportion of B in the cluster decreases the energy. When there are equal numbers of both molecules, the heterogeneous cluster energies reflect those of homogeneous A clusters across cluster sizes. However, changing the molecule proportions affects the cluster energies significantly in that $A_{30}B_{10}$ possesses a high energy while $A_{10}B_{30}$ has a significantly low energy, producing the highest and lowest energy clusters of all the cPAH clusters evaluated. This suggests that in all heterogeneous cases the presence of B increases cluster stability if its composition is above 50%.

These energy trends are in agreement with the structural metrics discussed previously, so that a higher degree of order within the heterogeneous cPAH clusters (increased stack formation as quantified by CNs, for example) corresponds to a greater interaction strength.

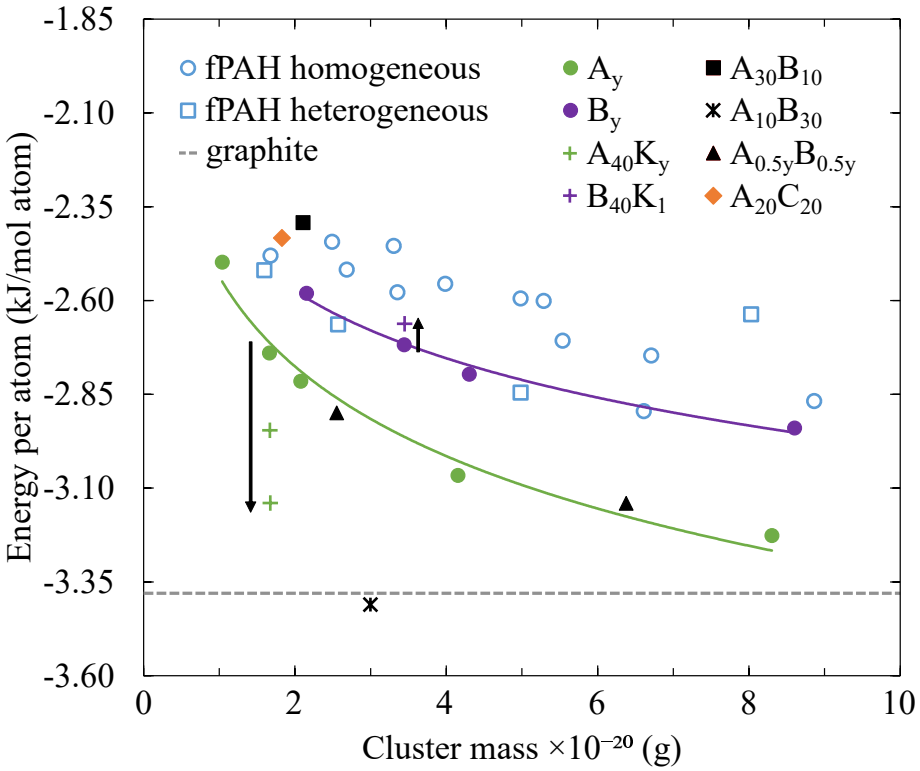

Figure 8: *Intermolecular energy per atom versus cluster mass for all clusters considered in this work. Lines are drawn for the cPAH homogeneous clusters to guide the eye and black arrows show the energy changes caused by the addition of a cation(s). The subscript y is used to denote an unspecified number of molecules in order to consider multiple clusters. The experimental binding energy of graphite [5] is shown as a horizontal dashed line.*

This highlights that the stacking of A within the bowls of B decreases the cluster intermolecular energy until a proportion (>50% A) at which the presence of A disrupts B stacking by inserting within columns instead of only residing between or at the ends of columns, thereby destabilising the cluster. These stable cPAH particles may present a potential nanostructure of soot particles but the enhanced cPAH-cPAH interactions are not sufficient to explain their rapid formation in flames.

3.3 How do complex cPAH systems self-assemble?

Many practical applications involve systems that contain many molecule types. Of particular interest to combustion and materials scientists are cPAH systems that also contain fPAHs or ions. We investigate relevant representative clusters using all of the metrics previously discussed to show the influence of different molecule curvatures and ion interactions within cPAH systems.

3.3.1 Particles containing cPAHs and fPAHs

To evaluate the self-assembly of clusters containing curved and flat PAHs, we consider $A_{20}C_{20}$. As seen in Figure 3, this cluster shows a distinct partitioning of the molecule types in a janus configuration, in contrast to the mixed arrangement seen in homogeneous clusters and the core-shell structure seen in heterogeneous clusters containing either fPAHs or cPAHs. The average intermolecular spacing of 0.43 nm (Table 1) comes almost entirely from neighbouring C and matches the spacing calculated for a homogeneous C cluster [17]. This suggests that the fPAH molecules orient in a stacked configuration, but the constituent cPAHs do not. This is highlighted in a detailed CN evaluation which shows constituent C have a CN of approximately 1.5 while A have no near neighbours within a stacked configuration cut-off radius (CN of 0.0), shown in Figure 4. These structural values agree with the respective homogeneous C and A clusters, as do the molecular alignment angles (see Supplementary Information Figure A4). The distinct types of local ordering cause the mixed fPAH and cPAH cluster to produce a janus particle with two different halves, highlighted by similar molecule type radial distances (see Table 1). This cluster containing both curved and flat PAHs has an energy similar to that of homogeneous cPAH clusters, indicating that the mixing of molecule types does not enhance molecule interaction energy and instead it remains similar to that of the weaker component.

Dispersive and electrostatic interactions dominate the attractive forces between homogeneous interactions of fPAHs and cPAHs. However, this mixed molecule system is hindered by sterics and mismatched polarities and thus produces weaker interactions and a relatively low density. In this way the stronger interactions between like molecules contribute to a particle system in which the two molecule types are immiscible. Many material systems, such as coal and soot particles, are seen experimentally to possess both curved and flat aromatics. These results suggest that when molecule type separation is not observed in such systems, self-assembly through physical interactions does not control the molecular structure. For example, covalent bonding between fPAHs and cPAHs may explain why soot particles do not form janus particles [54, 55]. These results are also of interest in developing janus colloidal systems where interesting flow dynamics and self-assembly are predicted [62, 83].

3.3.2 Particles containing cPAHs and ion(s)

We further explore the influence of heterogeneity by considering clusters containing 40 molecules (A or B) and one or two potassium cations. These systems can be directly compared to homogeneous systems of the same size. Potassium ions are selected because they are known to interact with cPAHs in systems of interest [68] and, importantly, because the intermolecular interactions between K^+ and cPAHs have already been parameterised within the curPAHIP potential [9]. As seen in Table 1, the inclusion of ion(s) within the cPAH clusters appears to increase the cluster diameter, and thus decrease the cluster density, slightly.

The cation(s) seems to have an effect on molecular arrangement that depends on the constituent cPAH size. The average CN of the B cluster decreases with the addition of K^+ (shown by a dotted arrow in Figure 4), suggesting a disruption of the highly stacked or-

dering in agreement with an increased intermolecular spacing. Conversely, the A clusters show increased ordering with a higher CN (dashed arrow in Figure 4) and decreased spacing. This effect increases with the addition of a second cation suggesting that the cation influence is additive, although the CNs are still lower than those of the B clusters. The addition of a potassium cation(s) also results in decreased average radial distances for both molecule types, so that average molecular distance values are around 75% of the total cluster radius. In agreement with these structural metrics, the presence of cation(s) in the cluster has opposite effects on cluster energies: B clusters with K^+ show an increased energy, while clusters with A containing K^+ showed a decreased energy in proportion with the number of ions. These differences are shown with black arrows in Figure 8, again showing that the presence of an ion(s) influences molecular interactions and cluster structure in different ways depending on the molecule size.

The majority of B within an ion-containing cluster remain in tilted stacks with the alignment angle distribution, seen in Figure 6 (bottom row), showing a dominant peak at 20°. Unlike the homogeneous B cluster, however, additional angles are present around 55° and 135°. This shows that the addition of a cation causes some disruption to the stacked structure otherwise seen in homogeneous or heterogeneous clusters containing B. This is visible in the cluster image in Figure 3, which shows that the $B_{40}K_1$ possesses more short stacks compared to the long columnar structure of B_{40}. The alignment angle distributions of A clusters containing K^+ are significantly different than the homogeneous and heterogeneous cases as well as the crystal structure, with a broadening and splitting of the 45° peak, shift and increase of a peak around 110°, and disappearance of high angles above 140°.

These quantitative differences suggest that the addition of a cation promotes stacking within the A cluster and disrupts the existing stacking within the B cluster. This can be observed in the cluster visualisations in Figure 3, which highlight the atoms immediately around the cation(s). All clusters show a solvation shell of four molecules around each cation with the cPAH electron-rich convex surfaces facing towards the cation(s). cPAHs form a tetrahedral-like formation, called a "flower“ motif in Bowal et al. [9], compared to the staggered triangular "propeller“ motif adopted by fPAHs around a cation [4]. Steric effects allow this motif to serve as a seed for the A structure while disrupting the long stacks otherwise present in B clusters. This indicates that the self-assembly behaviour around cations depends on the cPAHs considered and so the addition of cations does not always increase molecular alignment and stability in large homogeneous clusters. These results also support the idea that a small cluster of 1–5 cPAH can be stabilised as an ionic nuclei that could contribute to other mechanisms for soot nanoparticle formation [47].

4 Conclusions

Curved carbons are ubiquitous; understanding such systems holds great promise in many systems and applications such as pollution reduction, novel nanocarbon materials, and sensors. This work provides a first detailed exploration of the self-assembly of particles containing cPAHs, examining their nanostructure in homogeneous clusters containing one molecule type only, heterogeneous clusters containing different cPAH sizes and ratios, and

complex cPAH clusters containing fPAHs or cations. We extend the previously developed curPAHIP potential to capture the interactions between large cPAHs and mixed cPAH systems and allow the simulations necessary for this analysis. This work centres around three questions in materials and combustion science seeking to understand the ability of cPAHs to self-assemble into an ordered phase, the characteristics of the internal nanostructure of cPAH nanoparticles, and the influence of fPAHs and ions within cPAH systems.

We find that the presence of cPAHs generally disrupts mesophase formation, although the structures formed depend on the constituent cPAHs. Structural metrics, including intermolecular spacing, coordination number and alignment angles show that the nanostructure of homogeneous cPAH particles is dependent on molecule size but unaffected by particle size (from 2–5 nm). B form parallel stacked columns similar to fPAHs but with a distinct tilt in the molecular alignment angles. In contrast, A do not possess short-range order. Both homogeneous particle systems show similarities to the crystal structures of comparable cPAHs. Mixing of cPAH sizes influences the structure of a nanoparticle. The addition of A to a particle containing B serves to enhance the π-π stacking and interactions of A, resulting in lower energy particles. CN and energy values show that B clusters with some added A (<50%) form stable nanoparticles arranged in molecular stacks that have stronger intermolecular interactions than homogeneous and heterogeneous clusters containing cPAHs and/or fPAHs. Regardless of molecular ratio, heterogeneous cPAH particles show a core-shell type arrangement similar to the partitioning observed in fPAH particles but less distinct due to bowl complementarity. Particles containing cPAHs and fPAHs self-assemble into janus particles with minimal interaction between the molecule types, suggesting that the two molecule types are not miscible and may provide nanoparticles with interesting electronic properties. The addition of cations within cPAH particles causes the formation of a solvation shell that influences the internal particle structure. A show enhanced local order extending from the cation(s), while the stacked structure of B is disrupted due to the cation's presence.

This work provides a detailed evaluation of the molecular structure of cPAH-based nanoparticles. The systems evaluated are not exhaustive but serve as a guide for how composition, such as molecule curvature, size, ratio, type and number, influences nanoparticle self-assembly. This provides insight into the probable arrangement of curved aromatics within systems of interest to both ubiquitous natural materials and those developed for applications. Further work to thoroughly develop a fPAH-cPAH intermolecular potential and test the effect of molecular composition should be done to further explore the formation and potential applications of semi-polar janus particles containing cPAHs and fPAHs. In addition, future studies should examine the influence of ion charge, size and number on these structural properties. The presence of additional atoms within cPAHs should also be considered since the interactions between curved aromatic molecules containing heteroatoms, such as oxygen, show increased dimer interactions that provide further electrostatic stabilisation [13].

Acknowledgements

This work used the ARCHER UK National Supercomputing Service (http://www.archer.ac.uk). K.B. is grateful to the Cambridge Trust and King's College, Cambridge for their financial support. This project is also supported by the National Research Foundation (NRF), Prime Minister's Office, Singapore under its Campus for Research Excellence and Technological Enterprise (CREATE) programme.

A Supplementary Information

A.1 Molecule descriptions

Corannulene (A) geometry (x, y, z in nm) and charges, taken from Bowal et al. [9], are provided below.

```
35
CORANNULENE with curPAHIP charges
C     0.103   0.064   0.085    0.020
C     0.093  -0.078   0.085    0.020
C    -0.045  -0.112   0.085    0.020
C    -0.121   0.008   0.085    0.020
C    -0.030   0.117   0.085    0.020
C     0.205   0.129   0.022    0.177
C     0.310   0.049  -0.032   -0.201
C     0.300  -0.090  -0.032   -0.201
C     0.187  -0.156   0.022    0.177
C     0.143  -0.279  -0.032   -0.201
C     0.007  -0.313  -0.033   -0.201
C    -0.090  -0.225   0.022    0.177
C    -0.242   0.016   0.022    0.177
C    -0.296  -0.103  -0.032   -0.201
C    -0.222  -0.222  -0.032   -0.201
C    -0.280   0.142  -0.031   -0.201
C    -0.190   0.250  -0.031   -0.201
C    -0.059   0.235   0.023    0.177
C     0.049   0.310  -0.032   -0.201
C     0.178   0.258  -0.032   -0.201
H    -0.221   0.345  -0.072    0.133
H     0.031   0.408  -0.072    0.133
H     0.259   0.317  -0.073    0.133
H     0.398   0.097  -0.072    0.133
H     0.380  -0.149  -0.075    0.133
H     0.215  -0.348  -0.073    0.133
H    -0.024  -0.408  -0.074    0.133
H    -0.265  -0.312  -0.073    0.133
H    -0.396  -0.103  -0.074    0.133
H    -0.378   0.155  -0.073    0.133
X     0.103   0.064   0.132   -0.063
X     0.093  -0.078   0.132   -0.063
X    -0.045  -0.113   0.132   -0.063
X    -0.121   0.008   0.133   -0.063
X    -0.030   0.117   0.133   -0.063
```

The following atomic coordinates (in nm) and charges are used in this work for the $C_{42}H_{14}$

molecule (B).

```
66
2PENT15RING MOLECULE with curPAHIP charges
C    -0.200   0.000   0.135   -0.309
C    -0.317   0.000   0.043    0.425
C    -0.365  -0.132  -0.016   -0.126
C    -0.126  -0.124   0.159    0.041
C    -0.126   0.124   0.158    0.041
C     0.014   0.124   0.176    0.070
C     0.093   0.000   0.174   -0.190
C     0.014  -0.125   0.177    0.070
C     0.065  -0.244   0.122   -0.117
C    -0.486  -0.127  -0.098   -0.225
C    -0.543   0.000  -0.139    0.010
C    -0.486   0.127  -0.096   -0.225
C    -0.365   0.131  -0.016   -0.126
C    -0.277   0.252  -0.001    0.253
C    -0.162   0.242   0.091   -0.109
C    -0.044   0.318   0.073    0.039
C     0.065   0.244   0.122   -0.117
C     0.197   0.251   0.059    0.008
C     0.282   0.128   0.056    0.150
C     0.229   0.000   0.111    0.038
C    -0.029   0.421  -0.031    0.157
C     0.110   0.463  -0.060   -0.365
C     0.219   0.365  -0.036    0.346
C    -0.154   0.458  -0.100   -0.163
C    -0.275   0.373  -0.088   -0.210
C     0.284  -0.130   0.058    0.150
C     0.198  -0.252   0.060    0.008
C     0.401   0.126  -0.034   -0.116
C     0.347   0.366  -0.109   -0.392
C     0.435   0.249  -0.107   -0.017
C     0.220  -0.365  -0.036    0.346
H    -0.526   0.219  -0.137    0.128
H    -0.629   0.001  -0.205    0.090
H     0.369   0.449  -0.175    0.162
H     0.127   0.540  -0.134    0.161
H    -0.153   0.535  -0.176    0.116
H    -0.356   0.391  -0.157    0.133
C     0.402  -0.128  -0.032   -0.116
C     0.473   0.000  -0.054   -0.115
C     0.352  -0.369  -0.100   -0.392
C     0.437  -0.250  -0.105   -0.017
C    -0.278  -0.253   0.001    0.253
C    -0.162  -0.243   0.092   -0.109
```

```
C    -0.044  -0.318   0.072    0.039
C    -0.030  -0.418  -0.035    0.157
C     0.109  -0.458  -0.067   -0.365
C    -0.280  -0.378  -0.079   -0.210
C    -0.156  -0.455  -0.103   -0.163
H    -0.363  -0.398  -0.146    0.133
H    -0.153  -0.525  -0.186    0.116
H    -0.527  -0.218  -0.140    0.128
H     0.126  -0.534  -0.142    0.161
H     0.376  -0.453  -0.165    0.162
H     0.520  -0.246  -0.173    0.104
H     0.558  -0.001  -0.121    0.129
H     0.523   0.248  -0.171    0.104
X    -0.132   0.148   0.204    0.044
X    -0.170   0.266   0.137   -0.107
X    -0.051   0.340   0.119    0.041
X     0.060   0.267   0.169   -0.115
X     0.008   0.148   0.223    0.072
X    -0.050  -0.341   0.118    0.041
X    -0.169  -0.267   0.138   -0.107
X    -0.132  -0.148   0.205    0.044
X     0.060  -0.267   0.168   -0.115
X     0.009  -0.148   0.223    0.072
```

In both molecules, the element X represents the virtual massless atoms used to describe the flexoelectric effect, which are held above and parallel to the pentagon ring using intramolecular forces.

A.2 Density Functional Theory

Density functional theory calculations are used to determine the geometry of cPAH monomers and geometries and energies of cPAH dimers in order to assess the atomic and intermolecular descriptions employed in this work. The B97-D functional [29], a hybrid functional with an empirical dispersion correction, is used in this work. Geometry optimisations are carried at the B97-D/6-311G(d,p) level of theory with frequency calculations to ensure suitable minima are found, and subsequent single point calculations use B97-D/cc-pVTZ, with basis set superposition error corrections. These functional and basis sets were selected since they provide good agreement (within 4%) with benchmark CCSD(T) [37] and SAPT(DFT) [13] calculations of small cPAH molecules. The Gaussian 16 software is used for all DFT calculations [26].

A.3 Intermolecular potentials

The isoPAHAP and curPAHIP potentials take the following form,

$$U_{ab} = K\exp\left[-\alpha_{ab}\left(R_{ab}-\rho_{ab}\right)\right] - \left[1-\exp\left(-\beta R_{ab}\right)\sum_{k=0}^{6}\frac{\left(\beta R_{ab}\right)^{k}}{k!}\right]\frac{C_{6,ab}}{R_{ab}^{6}} + \frac{q_a q_b}{R_{ab}}, \quad \text{(A.1)}$$

where the first term is the short-range term in the Born–Mayer form, the second term is the dispersion term damped by the Tang-Toennies damping function [75] and the third is the point charge electrostatic term. U denotes the interaction energy between atom a and atom b, K sets the energy unit of this term and is taken as 0.001 hartree in this work, α is the hardness parameter in the Born–Mayer term, R_{ab} is the atom-atom separation where a and b denote atomic sites within a molecule, ρ_{ab} is a shape parameter, β is the damping coefficient, $C_{6,ab}$ is a dispersion coefficient, and q is the atomic point charge. Further details about the parametrisation and form of the isoPAHAP potential can be found in Totton et al. [77].

Table A1 provides the parameters of the curPAHIP intermolecular potential.

Table A1: *Parameters of curPAHIP in a.u.*

Atom pair	ρ	α	C_6
C C	5.6563	1.8783	30.282
C H	4.9320	1.7560	12.604
H H	4.1187	1.4043	5.2179

$\beta = 1.50$ a.u.

The following interaction parameters are used to describe systems containing K^+: $\sigma = 9.64$ and $\varepsilon = 3.43\times10^{-8}$ a.u. Further information on the development and parameters of the curPAHIP potential can be found in Bowal et al. [9].

A.4 Replica Exchange Molecular Dynamics simulation parameters

Replica temperatures for REMD simulations are selected using an exponential temperature distribution

$$T_w = T_0\exp(qw) \quad \text{(A.2)}$$

where T_w refers to the temperature (in K) at replica w, T_0 is the temperature (K) at replica 0 and q is a parameter which achieves the desired temperature range.

The temperature ranges are selected to encompass both solid- and liquid-like configurations. These temperature ranges differ with the molecular composition of the cluster, since constituent molecule sizes determine the temperature at which a cluster is liquid- or solid-like. The smallest molecule present determines the lower temperature bound, with A or C molecules at 200 K and B molecules at 400 K. Similarly the largest molecule present determines the upper temperature bound, with A or C molecules at $\geq$ 800 K and B molecules at $\geq$ 1600 K. The lowest and highest replica temperatures are listed for each cluster in Table A2.

The w and q parameters, also shown in Table A2, are selected for each cluster system to allow satisfactory exchange between replicas (discussed further below) using these temperature ranges.

Table A2: *Replica temperature selection parameters and temperature ranges (in K) for cPAH clusters considered in this work.*

Cluster	q	w	lowest T	highest T
A_{25}	0.054	0-26	200	≥ 800
A_{40}	0.050	0-29	200	≥ 800
A_{50}	0.040	0-35	200	≥ 800
A_{100}	0.025	0-59	200	≥ 800
A_{200}	0.017	0-86	200	≥ 800
B_{25}	0.045	0-32	400	≥ 1600
B_{40}	0.032	0-44	400	≥ 1600
B_{50}	0.030	0-47	400	≥ 1600
B_{100}	0.024	0-59	400	≥ 1600
$A_{20}B_{20}$	0.030	0-71	200	≥ 1600
$A_{50}B_{50}$	0.025	0-83	200	≥ 1600
$A_{30}B_{10}$	0.036	0-59	200	≥ 1600
$A_{10}B_{30}$	0.028	0-74	200	≥ 1600
$B_{40}K_1$	0.030	0-47	400	≥ 1600
$A_{40}K_1$	0.050	0-29	200	≥ 800
$A_{40}K_2$	0.050	0-29	200	≥ 1600

The effectiveness of an REMD simulation relies on the proper exchange of states between replicas so that the low temperature states are able to sample the high temperature configurations and vice versa. Replica exchange acceptance is a good indication of the movement between replicas and is a common indicator of simulation performance. Consistent acceptance values across the replicas indicate a good temperature selection for the system studied and an exchange acceptance of approximately 0.2 is found empirically and theoretically to provide the best accuracy for a given computational time [43, 59]. Exchange acceptances for simulations conducted in this work have an average between 0.20 and 0.35 with small system ranges, which indicates robust replica exchange with a good balance between equilibration within replicas and exchange between replicas. Replica exchange attempts are made every 100 fs, since frequent exchanges have been shown to increase efficiency without affecting the ensemble being sampled [69, 70].

A.5 Cut-off distance sensitivities

The selection of the cut-off distance, R, influences the calculated average intermolecular distances, coordination numbers and alignment angles. Due to the disordered molecular arrangements of the homogeneous A clusters (that is, sandwich-type stacking is not present), these results are the most sensitive to the selection of R.

Figure A1 shows the alignment angle distributions for all homogeneous clusters using four different cut-off distances. The influence of the cut-off distance is minimal in the B clusters, which show a very high proportion of molecules with at least one near neighbour at all cut-off distances (indicated by the inset percent values listed). At the higher cut-off distances, a second peak corresponding to further molecule layers (*i.e.* not the nearest neighbours alone) appears. The A clusters show some differences between angle distributions across the cut-off distances and the percent of molecules with a near neighbour increases dramatically between $R = 0.5$ nm and $R = 0.6$ nm. Note that for all systems, no neighbouring molecules are found using a cut-off distance of 0.4 nm or smaller.

Table A3 presents the average intermolecular distances of homogeneous clusters as a function of the cut-off distance used in our analysis. For the A clusters, the cut-off distance selected influences the average intermolecular distance calculated. Intuitively, an increase in the cut-off distance produces an increase in the average intermolecular distance, since the cut-off distance simply increases the range between 'neighbouring' molecules. At low cut-off values ($R = 0.5$ nm and $R = 0.6$ nm) very few molecule pairs exist and so these averages are not a clear picture of the true average intermolecular spacing throughout the cluster. At $R = 0.7$ nm, the majority of molecules ($\geq 95\%$) have at least one near neighbour and therefore this provides the best indication of the cluster average. In contrast, the cut-off distance does not have a large impact on the average intermolecular spacing of homogeneous B molecules. This highlights the highly stacked configuration of these molecules.

Table A3: *Average molecular intermolecular distance, in nm, for homogeneous clusters with varying cut-off values, R in nm, used.*

Cluster	Intermolecular distance (nm)			
	$R = 0.5$	$R = 0.6$	$R = 0.7$	$R = 0.8$
A_{25}	0.45	0.55	0.59	0.68
A_{40}	0.45	0.55	0.59	0.67
A_{50}	0.47	0.55	0.60	0.67
A_{100}	0.48	0.55	0.59	0.68
A_{200}	0.47	0.55	0.60	0.68
B_{25}	0.44	0.44	0.45	0.49
B_{40}	0.45	0.45	0.46	0.47
B_{50}	0.45	0.45	0.48	0.50
B_{100}	0.45	0.45	0.48	0.52

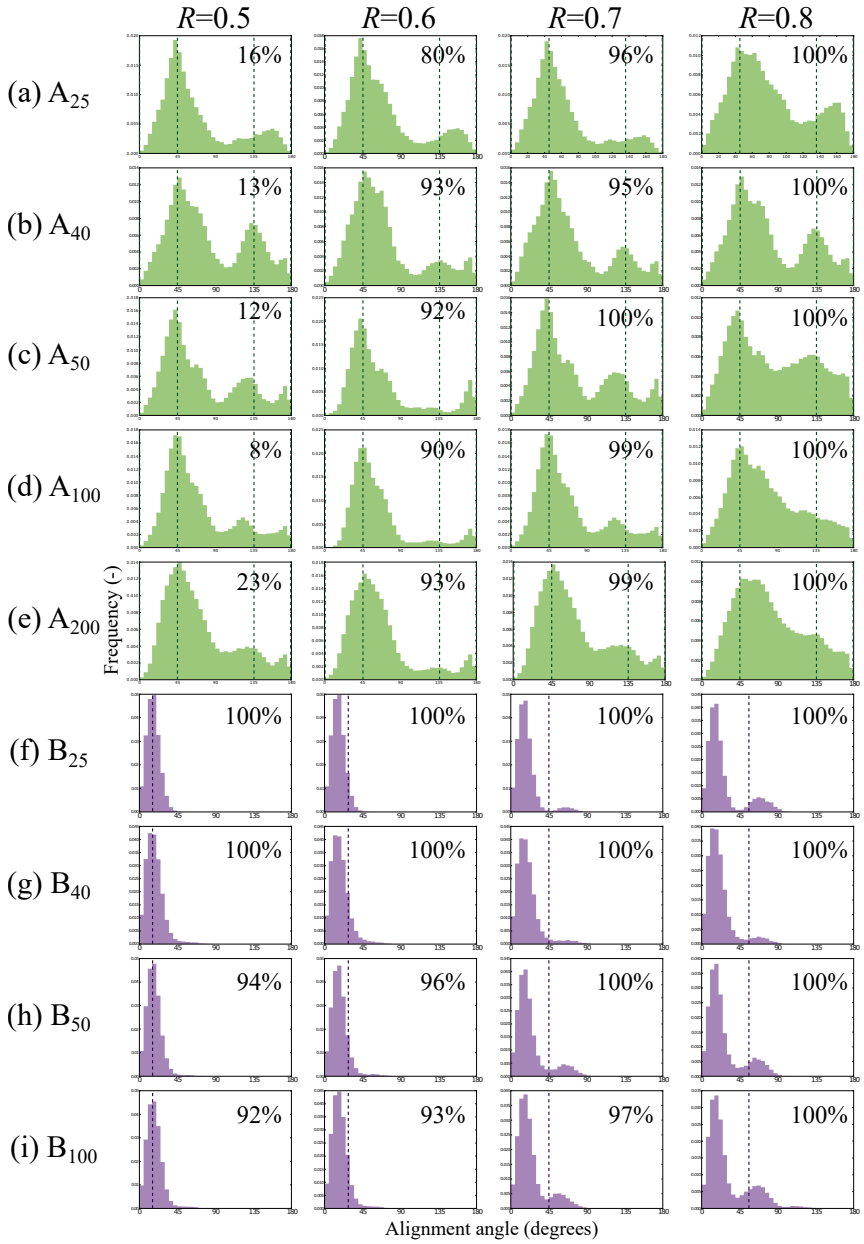

Figure A1: *Alignment angle distributions at different cut-off distances, R, in nm for the following clusters: (a) A_{25}, (b) A_{40}, (c) A_{50}, (d) A_{100}, (e) A_{200}, (f) B_{25}, (g) B_{40}, (h) B_{50}, (i) B_{100}. Dashed lines correspond to the A crystal structure (for (a)-(e)) and the minimised B dimer (for (f)-(i)). Percent values in the upper right hand corners of each angle distribution refer to the percent of molecules within the cluster that have at least one near neighbour.*

A.6 Calculation of radial distances and coordination numbers

Average radial distances and coordination numbers are calculated to provide insight into molecular arrangements and cluster structure. The average radial distance of molecule

type k, r_k, is calculated using the following equation:

$$r_k = \frac{1}{N_k} \sum_{m \in I_k} R_m, \tag{A.3}$$

where N_k is the number of molecules within $k \in \{\mathrm{A}, \mathrm{B}\}$, referring to the corannulene and $C_{42}H_{14}$ molecule types, I_k is the set of molecule indices within k and R_m is the radial distance between the cluster geometric centre and the geometric centre of molecule m. In this work, radial distances are calculated considering all atoms in the system.

The coordination number of molecule type k, CN_k, provides the average number of molecules within a distance $R^{(\mathrm{cutoff})}$. This is calculated as the average of the cumulative radial distribution function integrated over the centre of the cluster (set as the origin at 0) to a maximum cut-off radial distance, $R^{(\mathrm{cutoff})}$:

$$CN_k(R^{(\text{cut-off})}) = \frac{1}{N_k} \sum_{m \in I_k} \int_0^{R^{(\text{cut-off})}} \sum_{j=1}^{N_{\text{total}}} \delta(D_{mj} - R) dR \tag{A.4}$$

$k \in \{\mathrm{A}, \mathrm{B}, \mathrm{total}\}$ refers to the A molecules, B molecules and all curved molecules within the cluster, respectively. D_{mj} is the distance between the geometric centres of molecules m and j. This provides CN values from zero to two, corresponding to an isolated molecule and a molecule sandwiched between two others, respectively.

A.7 Corannulene crystal structure

Several of the structural metrics used in this paper were applied to the known crystal structure of corannulene in order to provide a benchmark and verify the calculations used. As early as 1975, it was shown through X-ray analysis that corannulene crystallises in a close-packed structure mostly stabilised through CH-π interactions, in space group $P2_1/c$ [30] (see Fig A2).

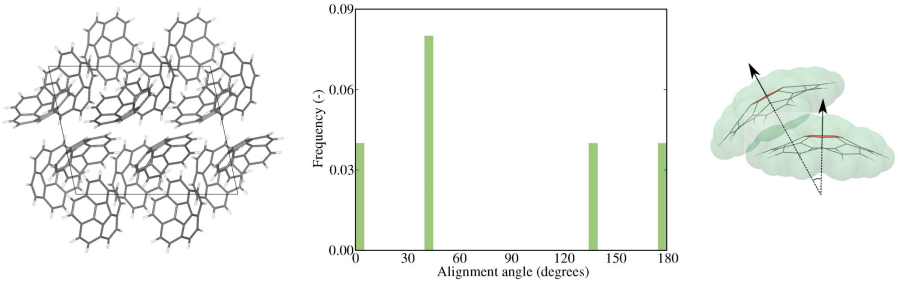

Figure A2: *Snapshot of corannulene crystal structure (left) with calculated alignment angle distribution (centre) and a schematic illustrating an alignment angle of* 30° *between two neighbouring A (right).*

A crystal structure containing 18 molecules from X-ray data provided by Petrukhina et al. [57] through the Cambridge Crystallographic Data Centre provides an independent verification of the analyses used in this work as well as a known experimental structure

useful for comparison. The average intermolecular spacing values calculated using our analysis methods are 0.57 nm, 0.72 nm, and 0.76 nm considering 1, 2, and 3 neighbouring molecules, respectively. These individual distances between corannulene monomers within the crystal structure calculated in our analysis are in excellent agreement with those reported in Sanyal et al. [65]. Figure A2 shows the crystal structure and alignment angles examined in this work.

A.8 Alignment angles

Alignment angle distributions are shown for large homogeneous and heterogenenous cPAH clusters (see Figure A3) and a cluster containing cPAHs and fPAHs (see Figure A4).

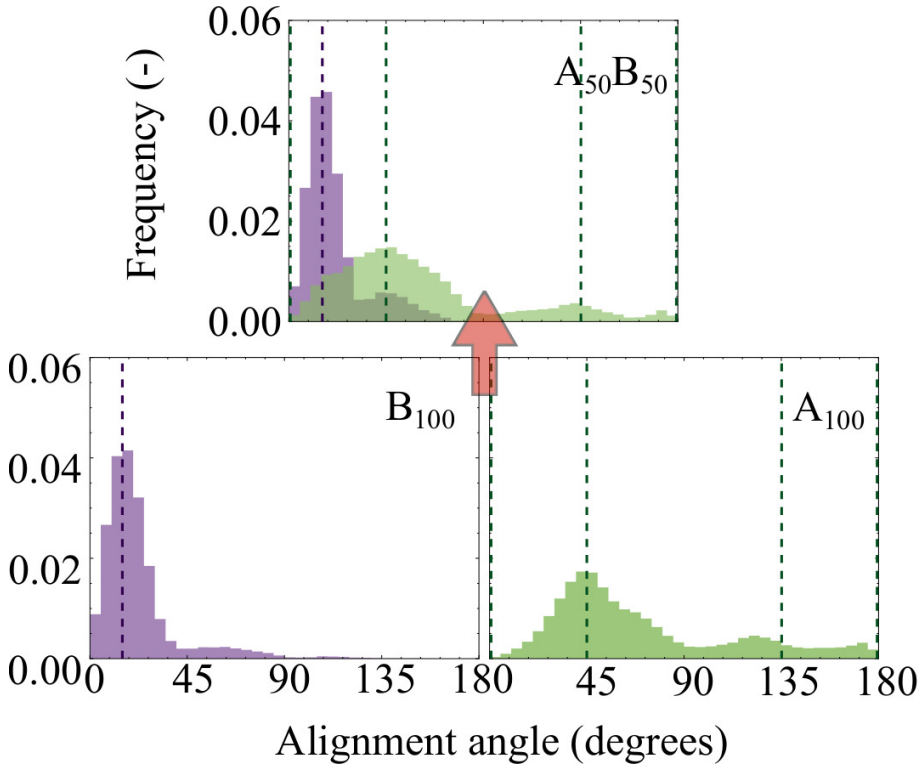

Figure A3: *Alignment angle distributions for homogeneous and heterogeneous A and B clusters each containing 100 molecules.*

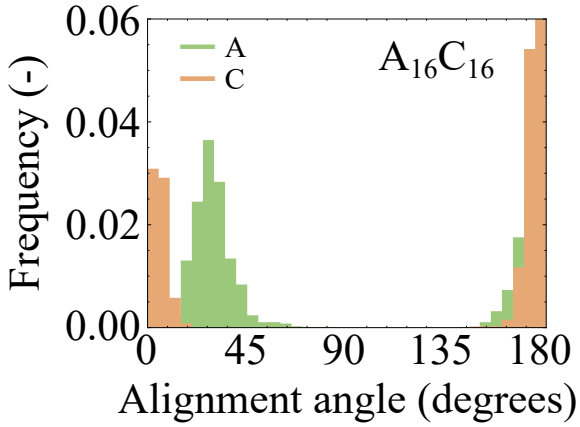

Figure A4: *Alignment angle distributions for the $A_{20}C_{20}$ cluster containing both cPAHs and fPAHs.*

References

[1] M. J. Abraham, T. Murtola, R. Schulz, S. Páll, J. C. Smith, B. Hess, and E. Lindah. GROMACS: High performance molecular simulations through multi-level parallelism from laptops to supercomputers. *SoftwareX*, 1-2:19–25, 2015. doi:10.1016/j.softx.2015.06.001.

[2] J. P. Abrahamson, A. Jain, A. C. van Duin, and R. L. Vander Wal. Carbon structure and the resulting graphitizability upon oxygen evolution. *Carbon*, 135:171–179, 2018. doi:10.1016/j.carbon.2018.04.055.

[3] B. Apicella, P. Pre, M. Alfè, A. Ciajolo, V. Gargiulo, C. Russo, A. Tregrossi, D. Deldique, and J. Rouzaud. Soot nanostructure evolution in premixed flames by high resolution electron transmission microscopy (hrtem). *Proceedings of the Combustion Institute*, 35(2):1895–1902, 2015. doi:10.1016/j.proci.2014.06.121.

[4] M. Bartolomei, F. Pirani, and J. Marques. Aggregation enhancement of coronene molecules by seeding with alkali-metal ions. *Physical Chemistry Chemical Physics*, 21(29):16005–16016, 2019. doi:10.1039/c9cp02658d.

[5] L. X. Benedict, N. G. Chopra, M. L. Cohen, A. Zettl, S. G. Louie, and V. H. Crespi. Microscopic determination of the interlayer binding energy in graphite. *Chemical Physics Letters*, 286(5-6):490–496, 1998. doi:10.1016/S0009-2614(97)01466-8.

[6] M. L. Botero, Y. Sheng, J. Akroyd, J. Martin, J. A. Dreyer, W. Yang, and M. Kraft. Internal structure of soot particles in a diffusion flame. *Carbon*, 141:635–642, 2019. doi:10.1016/j.carbon.2018.09.063.

[7] K. Bowal, J. W. Martin, and M. Kraft. Partitioning of polycyclic aromatic hydrocarbons in heterogeneous clusters. *Carbon*, 2018. doi:10.1016/j.carbon.2018.11.004.

[8] K. Bowal, P. Grancic, J. W. Martin, and M. Kraft. Sphere Encapsulated Monte Carlo: Obtaining minimum energy configurations of large aromatic systems. *The Journal of Physical Chemistry A*, 123(33):7303–7313, 2019. doi:10.1021/acs.jpca.9b04821.

[9] K. Bowal, J. W. Martin, A. J. Misquitta, and M. Kraft. Ion-induced soot nucleation using a new potential for curved aromatics. *Combustion Science and Technology*, 191(5-6):747–765, 2019. doi:10.1080/00102202.2019.1565496.

[10] K. Bowal, L. Pascazio, H. Wang, D. Chen, and M. Kraft. Surface properties of heterogeneous polycyclic aromatic hydrocarbon clusters. *Proceedings of the Combustion Institute*, 2020.

[11] H. E. Bronstein, N. Choi, and L. T. Scott. Practical synthesis of an open geodesic polyarene with a fullerene-type 6:6-double bond at the center: Diindeno[1,2,3,4-*defg*;1',2',3',4'-*mnop*]chrysene. *Journal of the American Chemical Society*, 124 (30):8870–8875, 2002. doi:10.1021/ja0123148.

[12] R. Byrd, P. Lu, J. Nocedal, and C. Zhu. A limited memory algorithm for bound constrained optimization. *SIAM Journal of Scientific Computing*, 16:1190–1208, 1995. doi:10.1137/0916069.

[13] E. M. Cabaleiro-Lago, B. Fernández, and J. Rodríguez-Otero. Dissecting the concave-convex π-π interaction in corannulene and sumanene dimers: SAPT(DFT) analysis and performance of DFT dispersion-corrected methods. *Journal of Computational Chemistry*, 39(2):93–104, 2018. doi:10.1002/jcc.25084.

[14] J. Camacho, C. Liu, C. Gu, H. Lin, Z. Huang, Q. Tang, X. You, C. Saggese, Y. Li, H. Jung, L. Deng, I. Wlokas, and H. Wang. Mobility size and mass of nascent soot particles in a benchmark premixed ethylene flame. *Combustion and Flame*, 162(10): 3810–3822, 2015. doi:10.1016/j.combustflame.2015.07.018.

[15] D. Chen and K. H. Luo. Reactive sites on the surface of polycyclic aromatic hydrocarbon clusters: A numerical study. *Combust. Flame*, 211:362–373, 2020. doi:10.1016/j.combustflame.2019.09.034.

[16] D. Chen and H. Wang. Cation-π interactions between flame chemiions and aromatic compounds. *Energy & Fuels*, 31(3):2345–2352, 2017. doi:10.1021/acs.energyfuels.6b02354.

[17] D. Chen, T. S. Totton, J. Akroyd, S. Mosbach, and M. Kraft. Phase change of polycyclic aromatic hydrocarbon clusters by mass addition. *Carbon*, 77:25–35, 2014. doi:10.1016/j.carbon.2014.04.089.

[18] D. Chen, T. S. Totton, J. Akroyd, S. Mosbach, and M. Kraft. Size-dependent melting of polycyclic aromatic hydrocarbon nano-clusters: A molecular dynamics study. *Carbon*, 67:79–91, 2014. doi:10.1016/j.carbon.2013.09.058.

[19] D. Chen, J. Akroyd, S. Mosbach, D. Opalka, and M. Kraft. Solid–liquid transitions in homogenous ovalene, hexabenzocoronene and circumcoronene clusters: A molecular dynamics study. *Combustion and Flame*, 162(2):486–495, 2015. doi:10.1016/j.combustflame.2014.07.025.

[20] M.-K. Chen, H.-J. Hsin, T.-C. Wu, B.-Y. Kang, Y.-W. Lee, M.-Y. Kuo, and Y.-T. Wu. Highly curved bowl-shaped fragments of fullerenes: Synthesis, structural analysis, and physical properties. *Chemistry–A European Journal*, 20(2):598–608, 2014. doi:10.1002/chem.201303357.

[21] B. Demir and M. Göktuğ Ahunbay. Adsorption of perfluorohexane in BAM-P109 type activated carbon via molecular simulation. *Adsorption Science & Technology*, 34(1):79–92, 2016. doi:10.1177/0263617415619535.

[22] M. A. Dobrowolski, A. Ciesielski, and M. K. Cyrański. On the aromatic stabilization of corannulene and coronene. *Physical Chemistry Chemical Physics*, 13(46):20557–20563, 2011.

[23] C. Dubceac, Y. Sevryugina, I. V. Kuvychko, O. V. Boltalina, S. H. Strauss, and M. A. Petrukhina. Self-assembly of aligned hybrid one-dimensional stacks from two complementary π-bowls. *Crystal Growth & Design*, 18(1):307–311, 2018. doi:10.1021/acs.cgd.7b01258.

[24] A. S. Filatov, L. T. Scott, and M. A. Petrukhina. π-π interactions and solid state packing trends of polycyclic aromatic bowls in the indenocorannulene family: Predicting potentially useful bulk properties. *Crystal Growth and Design*, 10(10):4607–4621, 2010. doi:10.1021/cg100898g.

[25] D. M. Forkey, S. Attar, B. C. Noll, R. Koerner, M. M. Olmstead, and A. L. Balch. Crystallographic characterization of the molecular structure and solid state packing of the fullerene-shaped hydrocarbon c36h12. *Journal of the American Chemical Society*, 119(24):5766–5767, 1997. doi:10.1021/ja970845j.

[26] M. J. Frisch, G. W. Trucks, H. B. Schlegel, G. E. Scuseria, M. A. Robb, J. R. Cheeseman, G. Scalmani, V. Barone, G. A. Petersson, H. Nakatsuji, X. Li, M. Caricato, A. V. Marenich, J. Bloino, B. G. Janesko, R. Gomperts, B. Mennucci, H. P. Hratchian, J. V. Ortiz, A. F. Izmaylov, J. L. Sonnenberg, D. Williams-Young, F. Ding, F. Lipparini, F. Egidi, J. Goings, B. Peng, A. Petrone, T. Henderson, D. Ranasinghe, V. G. Zakrzewski, J. Gao, N. Rega, G. Zheng, W. Liang, M. Hada, M. Ehara, K. Toyota, R. Fukuda, J. Hasegawa, M. Ishida, T. Nakajima, Y. Honda, O. Kitao, H. Nakai, T. Vreven, K. Throssell, J. A. Montgomery, Jr., J. E. Peralta, F. Ogliaro, M. J. Bearpark, J. J. Heyd, E. N. Brothers, K. N. Kudin, V. N. Staroverov, T. A. Keith, R. Kobayashi, J. Normand, K. Raghavachari, A. P. Rendell, J. C. Burant, S. S. Iyengar, J. Tomasi, M. Cossi, J. M. Millam, M. Klene, C. Adamo, R. Cammi, J. W. Ochterski, R. L. Martin, K. Morokuma, O. Farkas, J. B. Foresman, and D. J. Fox. Gaussian 16 Revision A.03, 2016. Gaussian Inc. Wallingford CT.

[27] S. Grabowsky, M. Weber, Y.-S. Chen, D. Lentz, B. M. Schmidt, M. Hesse, and P. Luger. Electron density of corannulene from synchrotron data at 12 K, comparison with fullerenes. *Zeitschrift für Naturforschung B*, 65(4):452–460, 2010. doi:10.1515/znb-2010-0403.

[28] P. Grančič, J. W. Martin, D. Chen, S. Mosbach, and M. Kraft. Can nascent soot particles burn from the inside? *Carbon*, 109:608–615, 2016. doi:10.1016/j.carbon.2016.08.025.

[29] S. Grimme. Semiempirical GGA-type density functional constructed with a long-range dispersion correction. *Journal of Computational Chemistry*, 27(15):1787–1799, 2006. doi:10.1002/jcc.20495.

[30] J. C. Hanson and C. Nordman. The crystal and molecular structure of corannulene, c20h10. *Acta Crystallographica Section B: Structural Crystallography and Crystal Chemistry*, 32(4):1147–1153, 1976. doi:10.1107/S0567740876012430.

[31] P. J. Harris. New perspectives on the structure of graphitic carbons. *Critical Reviews in Solid State and Materials Sciences*, 30(4):235–253, 2005. doi:10.1080/10408430500406265.

[32] J. Hernández-Rojas, F. Calvo, S. Niblett, and D. Wales. Dynamics and thermodynamics of the coronene octamer described by coarse-grained potentials. *Physical Chemistry Chemical Physics*, 19(3):1884–1895, 2017. doi:10.1039/C6CP07671H.

[33] K. Hukushima and K. Nemoto. Exchange Monte Carlo method and application to spin glass simulations. *Journal of the Physical Society of Japan*, 65(6):1604–1608, 1996. doi:10.1143/JPSJ.65.1604.

[34] W. Humphrey, A. Dalke, and K. Schulten. VMD: Visual molecular dynamics. *Journal of Molecular Graphics*, 14(1):33–38, 1996. doi:10.1016/0263-7855(96)00018-5.

[35] K. Imamura, K. Takimiya, T. Otsubo, and Y. Aso. Triphenyleno[1,12-*bcd*: 4,5-*b*'c'd':8,9-*b*"c"d"]trithiophene: the first bowl-shaped heteroaromatic. *Chemical Communications*, 18:1859–1860, 1999. doi:10.1039/A905860E.

[36] T. Janowski, A. R. Ford, and P. Pulay. Accurate correlated calculation of the intermolecular potential surface in the coronene dimer. *Molecular Physics*, 108(3-4): 249–257, 2010. doi:10.1080/00268970903397249.

[37] T. Janowski, P. Pulay, A. S. Karunarathna, A. Sygula, and S. Saebø. Convex–concave stacking of curved conjugated networks: Benchmark calculations on the corannulene dimer. *Chemical Physics Letters*, 512(4-6):155–160, 2011. doi:10.1016/j.cplett.2011.07.030.

[38] K. Johansson, F. El Gabaly, P. Schrader, M. Campbell, and H. Michelsen. Evolution of maturity levels of the particle surface and bulk during soot growth and oxidation in a flame. *Aerosol Science and Technology*, 51(12):1333–1344, 2017. doi:10.1080/02786826.2017.1355047.

[39] G. A. Kaminski, R. A. Friesner, J. Tirado-Rives, and W. L. Jorgensen. Evaluation and reparametrization of the OPLS-AA force field for proteins via comparison with accurate quantum chemical calculations on peptides. *The Journal of Physical Chemistry B*, 105(28):6474–6487, 2001. doi:10.1021/jp003919d.

[40] E. Kanao, T. Kubo, T. Naito, T. Matsumoto, T. Sano, M. Yan, and K. Otsuka. Differentiating π interactions by constructing concave/convex surfaces using a bucky bowl molecule, corannulene in liquid chromatography. *Analytical chemistry*, 91(3): 2439–2446, 2018. doi:10.1021/acs.analchem.8b05260.

[41] M. R. Kennedy, L. A. Burns, and C. D. Sherrill. Buckyplates and buckybowls: Examining the effects of curvature on π–π interactions. *The Journal of Physical Chemistry A*, 116(48):11920–11926, 2012. doi:10.1021/jp305700k.

[42] R. Khanna, V. Sahajwalla, and R. H. Hurt. An atomistic technique for simulating non-covalent interactions in large ensembles of high-molecular-weight polyaromatics. *Carbon*, 43(1):67 – 77, 2005. doi:10.1016/j.carbon.2004.08.023.

[43] A. Kone and D. A. Kofke. Selection of temperature intervals for parallel-tempering simulations. *J. Chem. Phys.*, 122(20):206101, 2005. doi:10.1063/1.1917749.

[44] C. Liu, A. V. Singh, C. Saggese, Q. Tang, D. Chen, K. Wan, M. Vinciguerra, M. Commodo, G. De Falco, P. Minutolo, et al. Flame-formed carbon nanoparticles exhibit quantum dot behaviors. *Proceedings of the National Academy of Sciences*, 116(26):12692–12697, 2019. doi:10.1073/pnas.1900205116.

[45] F. J. Lovas, R. J. McMahon, J. U. Grabow, M. Schnell, J. Mack, L. T. Scott, and R. L. Kuczkowski. Interstellar chemistry: A strategy for detecting polycyclic aromatic hydrocarbons in space. *Journal of the American Chemical Society*, 127(12):4345–4349, 2005. doi:10.1021/ja0426239.

[46] J. W. Martin, R. I. Slavchov, E. K. Yapp, J. Akroyd, S. Mosbach, and M. Kraft. The polarization of polycyclic aromatic hydrocarbons curved by pentagon incorporation: The role of the flexoelectric dipole. *Journal of Physical Chemistry C*, 121(48): 27154–27163, 2017. doi:10.1021/acs.jpcc.7b09044.

[47] J. W. Martin, M. Botero, R. I. Slavchov, K. Bowal, J. Akroyd, S. Mosbach, and M. Kraft. Flexoelectricity and the formation of carbon nanoparticles in flames. *The Journal of Physical Chemistry C*, 122(38):22210–22215, 2018. doi:10.1021/acs.jpcc.8b08264.

[48] J. W. Martin, K. Bowal, A. Menon, R. I. Slavchov, J. Akroyd, S. Mosbach, and M. Kraft. Polar curved polycyclic aromatic hydrocarbons in soot formation. *Proceedings of the Combustion Institute*, 18:1–7, 2018. doi:10.1016/j.proci.2018.05.046.

[49] J. W. Martin, C. de Tomas, I. Suarez-Martinez, M. Kraft, and N. A. Marks. Topology of disordered 3D graphene networks. *Physical Review Letters*, 123(11):116105, 2019. doi:10.1103/PhysRevLett.123.116105.

[50] J. W. Martin, L. Nyadong, C. Ducati, M. Manley-Harris, A. G. Marshall, and M. Kraft. Nanostructure of gasification charcoal (biochar). *Environmental science & technology*, 53(7):3538–3546, 2019. doi:10.1021/acs.est.8b06861.

[51] L. Martinez, R. Andrade, E. G. Birgin, and J. M. Martinez. PACKMOL: A package for building initial configurations for molecular dynamics simulations. *Journal of Computational Chemistry*, 30(13):2157–2164, 2009. doi:10.1002/jcc.21224.

[52] A. Menon, J. A. Dreyer, J. W. Martin, J. Akroyd, J. Robertson, and M. Kraft. Optical band gap of cross-linked, curved, and radical polyaromatic hydrocarbons. *Physical Chemistry Chemical Physics*, 21(29):16240–16251, 2019. doi:10.1039/C9CP02363A.

[53] L. Pascazio, M. Sirignano, and A. D'Anna. Simulating the morphology of clusters of polycyclic aromatic hydrocarbons: The influence of the intermolecular potential. *Combustion and Flame*, 185:53–62, 2017. doi:10.1016/j.combustflame.2017.07.003.

[54] L. Pascazio, J. W. Martin, M. L. Botero, M. Sirignano, A. D'Anna, and M. Kraft. Mechanical properties of soot particles: The impact of crosslinked polycyclic aromatic hydrocarbons. *Combustion Science and Technology*, pages 1–21, 2019.

[55] L. Pascazio, J. W. Martin, K. Bowal, J. Akroyd, and M. Kraft. Exploring the internal structure of soot particles using nanoindentation: A reactive molecular dynamics study. *Combustion and Flame*, 219:45–56, 2020.

[56] M. A. Petrukhina, K. W. Andreini, L. Peng, and L. T. Scott. Hemibuckminsterfullerene $C_{30}H_{12}$: X-ray crystal structures of the parent hydrocarbon and of the two-dimensional organometallic network $\{[Rh_2(O_2CCF_3)_4]_3(C_{30}H_{12})\}$. *Angewandte Chemie International Edition*, 43(41):5477–5481, 2004. doi:10.1002/anie.200460855.

[57] M. A. Petrukhina, K. W. Andreini, J. Mack, and L. T. Scott. X-ray quality geometries of geodesic polyarenes from theoretical calculations: What levels of theory are reliable? *Journal of Organic Chemistry*, 70(14):5713–5716, 2005. doi:10.1021/jo050233e.

[58] M. Rapacioli, F. Calvo, F. Spiegelman, C. Joblin, and D. J. Wales. Stacked clusters of polycyclic aromatic hydrocarbon molecules. *The Journal of Physical Chemistry A*, 109(11):2487–2497, 2005. doi:10.1021/jp046745z.

[59] N. Rathore, M. Chopra, and J. J. De Pablo. Optimal allocation of replicas in parallel tempering simulations. *J. Chem. Phys.*, 122(10):24111–174903, 2005. doi:10.1063/1.1831273.

[60] A. M. Rice, E. A. Dolgopolova, B. J. Yarbrough, G. A. Leith, C. R. Martin, K. S. Stephenson, R. A. Heugh, A. J. Brandt, D. A. Chen, S. G. Karakalos, et al. Stack the bowls: Tailoring the electronic structure of corannulene-integrated crystalline materials. *Angewandte Chemie International Edition*, 57(35):11310–11315, 2018. doi:10.1002/anie.201806202.

[61] L. M. Roch, L. Zoppi, J. S. Siegel, and K. K. Baldridge. Indenocorannulene-based materials: Effect of solid-state packing and intermolecular interactions on optoelectronic properties. *The Journal of Physical Chemistry C*, 121(2):1220–1234, 2017. doi:10.1021/acs.jpcc.6b10895.

[62] S. Safaei, S. C. Hendy, and G. R. Willmott. Stability of amphiphilic janus dimers in shear flow: a molecular dynamics study. *Soft Matter*, 16(30):7116–7125, 2020.

[63] H. Sakurai, T. Daiko, H. Sakane, T. Amaya, and T. Hirao. Structural elucidation of sumanene and generation of its benzylic anions. *Journal of the American Chemical Society*, 127(33):11580–11581, 2005. doi:10.1021/ja0518169.

[64] M. F. Sanner, A. J. Olson, and J.-C. Spehner. Reduced surface: An efficient way to compute molecular surfaces. *Biopolymers*, 38(3):305–320, 1996. doi:10.1002/(SICI)1097-0282(199603)38.

[65] S. Sanyal, A. K. Manna, and S. K. Pati. Functional corannulene: diverse structures, enhanced charge transport, and tunable optoelectronic properties. *ChemPhysChem*, 15(5):885–893, 2014. doi:10.1002/cphc.201301050.

[66] L. Scanlon, P. Balbuena, Y. Zhang, G. Sandi, C. Back, W. Feld, J. Mack, M. Rottmayer, and J. Riepenhoff. Investigation of corannulene for molecular hydrogen storage via computational chemistry and experimentation. *The Journal of Physical Chemistry B*, 110(15):7688–7694, 2006. doi:10.1021/jp0574403.

[67] L. T. Scott, H. E. Bronstein, D. V. Preda, R. B. Ansems, M. S. Bratcher, and S. Hagen. Geodesic polyarenes with exposed concave surfaces. *Pure and applied chemistry*, 71(2):209–219, 1999. doi:10.1021/ar950197d.

[68] J. Simonsson, N. E. Olofsson, H. Bladh, M. Sanati, and P. E. Bengtsson. Influence of potassium and iron chloride on the early stages of soot formation studied using imaging LII/ELS and TEM techniques. *Proceedings of the Combustion Institute*, 36 (1):853–860, 2017. doi:10.1016/j.proci.2016.07.003.

[69] D. Sindhikara, Y. Meng, and A. E. Roitberg. Exchange frequency in replica exchange molecular dynamics. *The Journal of Chemical Physics*, 128(2):01B609, 2008. doi:10.1063/1.2816560.

[70] D. J. Sindhikara, D. J. Emerson, and A. E. Roitberg. Exchange often and properly in replica exchange molecular dynamics. *Journal of Chemical Theory and Computation*, 6(9):2804–2808, 2010. doi:10.1021/ct100281c.

[71] A. J. Stone, A. Dullweber, O. Engkvist, E. Fraschini, M. P. Hodges, A. W. Meredith, P. L. A. Popelier, and D. J. Wales. ORIENT: a program for studying interactions between molecules, version 4.9. 2017.

[72] Y. Sugita and Y. Okamoto. Replica-exchange molecular dynamics method for protein folding. *Chemical Physics Letters*, 314:141–151, 1999. doi:10.1016/S0009-2614(99)01123-9.

[73] A. Sygula and S. Saebø. π-π stacking of curved carbon networks: The corannulene dimer. *International Journal of Quantum Chemistry*, 109(1):65–72, 2009. doi:10.1002/qua.21794.

[74] A. Sygula, H. E. Folsom, R. Sygula, A. H. Abdourazak, Z. Marcinow, F. R. Fronczek, and P. W. Rabideau. Bowl stacking in curved polynuclear aromatic hydrocarbons: crystal and molecular structure of cyclopentacorannulene. *Journal of the Chemical Society, Chemical Communications*, 22:2571–2572, 1994. doi:10.1039/C39940002571.

[75] K. T. Tang and J. P. Toennies. An improved simple model for the van der Waals potential based on universal damping functions for the dispersion coefficients. *The Journal of Chemical Physics*, 80:3726–3741, 1984. doi:10.1063/1.447150.

[76] T. S. Totton, D. Chakrabarti, A. J. Misquitta, M. Sander, D. J. Wales, and M. Kraft. Modelling the internal structure of nascent soot particles. *Combustion and Flame*, 157(5):909–914, 2010. doi:10.1016/j.combustflame.2009.11.013.

[77] T. S. Totton, A. J. Misquitta, and M. Kraft. A first principles development of a general anisotropic potential for polycyclic aromatic hydrocarbons. *Journal of Chemical Theory and Computation*, 6(3):683–695, 2010. doi:10.1021/ct9004883.

[78] T. S. Totton, A. J. Misquitta, and M. Kraft. A quantitative study of the clustering of polycyclic aromatic hydrocarbons at high temperatures. *Physical Chemistry Chemical Physics*, 14(14):4081–4094, 2012. doi:10.1039/c2cp23008a.

[79] L. Verlet. Computer "experiments" on classical fluids. I. Thermodynamical properties of Lennard-Jones molecules. *Physical Review*, 159(1):98–103, 1967. doi:10.1103/PhysRev.159.98.

[80] B.-T. Wang, M. A. Petrukhina, and E. R. Margine. Electronic transport properties of selected carbon π-bowls with different size, curvature and solid state packing. *Carbon*, 94:174–180, 2015. doi:10.1016/j.carbon.2015.06.041.

[81] C. Wang, T. Huddle, C.-H. Huang, W. Zhu, R. L. Vander Wal, E. H. Lester, and J. P. Mathews. Improved quantification of curvature in high-resolution transmission electron microscopy lattice fringe micrographs of soots. *Carbon*, 117:174–181, 2017. doi:10.1016/j.carbon.2017.02.059.

[82] Y.-T. Wu and J. S. Siegel. Aromatic molecular-bowl hydrocarbons: synthetic derivatives, their structures, and physical properties. *Chemical reviews*, 106(12):4843–4867, 2006. doi:10.1021/cr050554q.

[83] J. Zhang, B. A. Grzybowski, and S. Granick. Janus particle synthesis, assembly, and application. *Langmuir*, 33(28):6964–6977, 2017.

[84] Y. Zhang, J. Zhuo, Y. Wu, and Q. Yao. Molecular simulation of the adsorption behaviors of CO_2/CH_4 in curvature, planar, and mixture models. *Energy & Fuels*, 34(4):4153–4161, 2020. doi:10.1021/acs.energyfuels.9b04418.

[85] Z. Zhang, J. Zhang, N. Chen, and L. Qu. Graphene quantum dots: an emerging material for energy-related applications and beyond. *Energy & Environmental Science*, 5(10):8869–8890, 2012. doi:10.1039/C2EE22982J.

[86] Q. Zhong, Q. Mao, L. Zhang, J. Xiang, J. Xiao, and J. P. Mathews. Structural features of Qingdao petroleum coke from HRTEM lattice fringes: Distributions of length, orientation, stacking, curvature, and a large-scale image-guided 3D atomistic representation. *Carbon*, 129:790–802, 2018. doi:10.1016/j.carbon.2017.12.106.